

1

2

CLD - a detector concept for FCC-ee

3

4

5

6

Author list under construction^{*}, N. Alipour Tehrani^{*}, N. Bacchetta^{*}, J.-J. Blaising[†],
E. Brondolin^{*}, M. Dam[§], D. Dannheim^{*}, K. Elsener^{*}, D. Hynds^{*}, P. Janot^{*}, A.M. Kolano^{*},
E. Leogrande^{*}, L. Linssen^{*}, A. Nürnberg^{*}, E.F. Perez^{*}, E. Perez Codina^{*}, M. Petric^{*},
P. Roloff^{*}, A. Sailer^{*}, N. Siegrist^{*}, O. Viazlo^{*}, G.G. Voutsinas^{*}, M.A. Weber^{*}

7

^{*} CERN, Geneva, Switzerland, [†] LAPP, Annecy, France, [§] Niels Bohr Institute, Copenhagen, Denmark

8

Abstract

9

10

11

12

13

14

15

16

This note gives a conceptual description and illustration of the CLD concept, based on the work on a detector at CLIC. CLD is one of the detectors envisaged at a future 100 km e^+e^- circular collider (FCC-ee). The note also contains a brief description of the simulation and reconstruction tools used in the linear collider community, which have been adapted for physics performance studies of CLD. The detector performance is described in terms of single particles, particles in jets, jet energy resolution and flavour tagging. The impact of beam-related backgrounds (incoherent pairs and synchrotron radiation photons) on the performance is also briefly discussed.

17

18	Contents	
19	1 Introduction	3
20	2 Overall Dimensions and Parameters	3
21	3 Vertex Detector	6
22	3.1 Overview and Layout	6
23	3.2 Beam-Induced Backgrounds in the Vertex Detector Region	7
24	3.3 Technology Choices, Cooling and Material Budget	8
25	4 Tracking System	11
26	4.1 Overview and Layout	11
27	4.2 Beam-Induced Backgrounds in the Tracking Region	13
28	4.3 Technology Choices and Cooling	14
29	5 Calorimetry	18
30	5.1 Introduction	18
31	5.2 Electromagnetic Calorimeter	18
32	5.3 Hadronic Calorimeter	21
33	5.4 Technology Choices and Cooling	22
34	6 Magnet System	24
35	6.1 Superconducting Solenoid	24
36	6.2 Yoke and Muon Detectors	24
37	7 Physics Performance	27
38	7.1 Simulation and Reconstruction	27
39	7.1.1 Event Generation	27
40	7.1.2 Detector Simulation	27
41	7.1.3 Event Reconstruction	27
42	7.1.4 Treatment of Background	28
43	7.2 Performance of Lower Level Physics Observables	29
44	7.2.1 Single Particle Performances	29
45	7.2.2 Performances for Complex Events	40
46	7.2.3 Jet Energy Resolution	45
47	7.2.4 Flavour Tagging	47
48	8 Summary and Outlook	47
49	9 Appendix I: Overview of CLD sub-detector parameters and read-out channel numbers	48

1 Introduction

The following sections describe a possible future detector for FCC-ee. This detector is derived from the most recent CLIC detector model [1], which features a silicon pixel vertex detector and a silicon tracker, followed by highly granular calorimeters (a silicon-tungsten ECAL and a scintillator-steel HCAL). A superconducting solenoid provides a strong magnetic field, and a steel yoke interleaved with RPC muon chambers closes the field.

The new detector model is dubbed "CLD". The overall parameters and all the subdetectors are described in this note, and the results of full simulation studies illustrate the detector performance for lower level physics observables.

The complex inner region (the Machine-Detector Interface MDI) with the beams crossing at an angle of 30 mrad, the final quadrupoles, screening and compensating solenoids and the luminosity monitor is described in dedicated chapters of the FCC CDR [2] and is not touched upon here. Instead, a forward region (cone) with an opening angle of 150 mrad is reserved for the MDI elements, in the CLD detector model.

At this stage of the conceptual design, it is assumed that the detector is identical for all the collision energies of FCC-ee, i.e. for Z (91 GeV c.m.), W (160 GeV), H (240 GeV) and top (365 GeV).

This note is structured as follows: In section 2, the overall layout of the CLD detector is described. Section 3 and 4 give details of the vertex and tracking detectors, while section 5 describes the calorimeters. The magnet system including the muon detectors is described in section 6. An overview of the simulation and reconstruction tools is given in section 7. These full simulation tools are used for an assessment of the CLD detector performances, results are also shown in section 7. Appendix I contains a table with the sensor areas of each sub-detector system, the pixel/pad sizes and the resulting total number of channels.

2 Overall Dimensions and Parameters

This section provides information about the general considerations leading to the choice of the main detector parameters. The starting point for the CLD concept was CLICdet [1], optimised for a 3 TeV linear collider, and which itself evolved out of the physics and detector studies performed for the CLIC CDR [3].

Some important constraints are given by the studies performed for the MDI at FCC-ee [4]:

- the need for a compensating solenoid near the interaction point limits the detector solenoidal field to a maximum of 2 Tesla;
- considerations of synchrotron radiation backgrounds, higher-order mode studies and vacuum requirements define the dimensions of the central beam pipe (radius 15 mm, half-length 125 mm);
- experience from the Stanford Linear Collider [5] indicates that the beam pipe needs to be water-cooled; this is approximated by a 1.2 mm thick Be beam pipe in the simulation model of CLD (0.8 mm for the beam pipe wall thickness, 0.4 mm as the equivalent thickness for the water cooling needed);
- furthermore, a gold layer of 5 μm thickness is required on the inside of the beam pipe;
- the space inside a 150 mrad cone is needed for accelerator and MDI elements and can not be used for detectors (other than the luminosity monitor (LumiCal)).

An additional major constraint stems from the continuous operation of a circular collider like FCC: power-pulsing as foreseen for almost all CLIC detector elements is not possible at FCC. The impact

92 on cooling needs and material budgets will depend on technology choices - this issue is discussed for
 93 each subdetector in the corresponding section of this document. Detailed engineering studies would be
 94 needed, but are beyond the scope of a conceptual detector design. Where possible, approximations based
 95 on "best guess" estimates are introduced for the material budget of CLD subdetectors.

96 The CLICdet model was adapted for FCC including two major steps:

- 97 • the radius of the silicon tracker was enlarged from 1.5 m to 2.15 m to compensate for the lower
 98 detector solenoid field (2 T instead of 4 T);
- 99 • the depth of the hadronic calorimeter was reduced to account for the lower maximum energy at
 100 FCC-ee ($5.5 \lambda_1$ instead of $7.5 \lambda_1$).

101 A comparison of the main parameters in the CLD and the CLICdet detector models is presented in
 102 Table 1. An illustration of the CLD concept is given in Figures 1 and 2.

Table 1: Comparison of key parameters of CLD and CLICdet detector models. The inner radius of the calorimeters is given by the smallest distance of the calorimeter (dodecagon) to the main detector axis.

Concept	CLICdet	CLD
Vertex inner radius [mm]	31	17
Tracker technology	Silicon	Silicon
Tracker half length [m]	2.2	2.2
Tracker outer radius [m]	1.5	2.1
Inner tracker support cylinder radius [m]	0.575	0.675
ECAL absorber	W	W
ECAL X_0	22	22
ECAL barrel r_{\min} [m]	1.5	2.15
ECAL barrel Δr [mm]	202	202
ECAL endcap z_{\min} [m]	2.31	2.31
ECAL endcap Δz [mm]	202	202
HCAL absorber	Fe	Fe
HCAL λ_1	7.5	5.5
HCAL barrel r_{\min} [m]	1.74	2.40
HCAL barrel Δr [mm]	1590	1166
HCAL endcap z_{\min} [m]	2.4	2.4
HCAL endcap Δz [mm]	1590	1166
Solenoid field [T]	4	2
Solenoid bore radius [m]	3.5	3.7
Solenoid length [m]	8.3	7.4
Overall height [m]	12.9	12.0
Overall length [m]	11.4	10.6

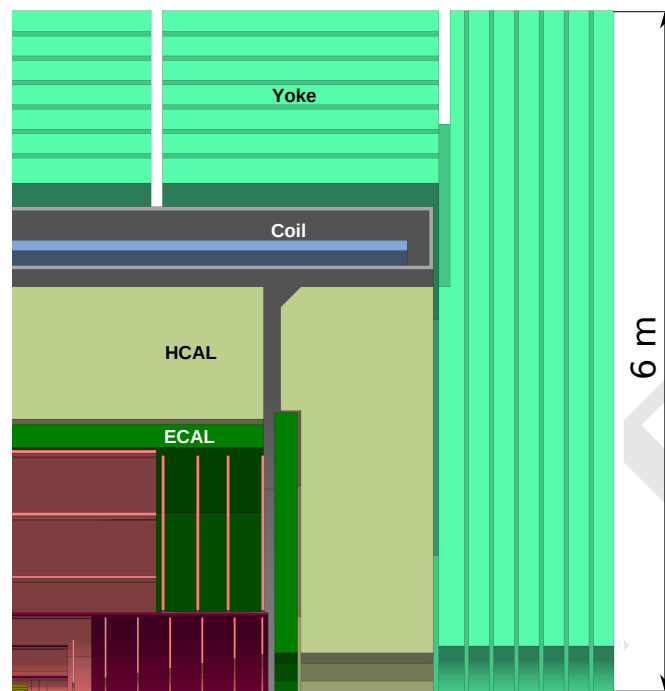


Figure 1: Vertical cross section showing the top right quadrant of CLD. Details of the MDI region are not shown.

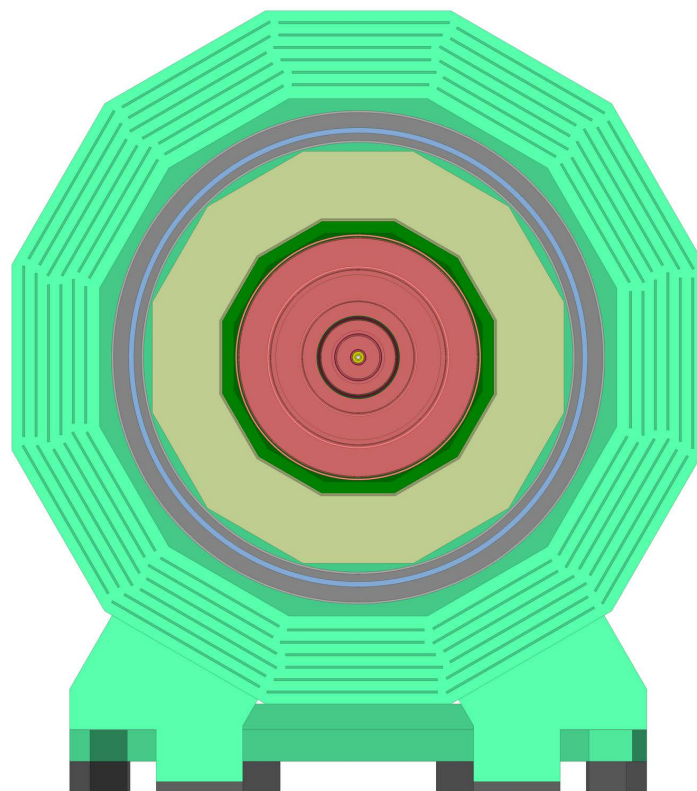


Figure 2: Transverse (XY) cross section of CLD.

3 Vertex Detector

3.1 Overview and Layout

The vertex detector in the CLD concept, a scaled version of the one in CLICdet, consists of a cylindrical barrel detector closed off in the forward directions by discs. The layout is based on double layers, i.e. two sensitive layers fixed on a common support structure (which includes cooling circuits). The barrel consists of three double layers, the forward region is covered by three sets of double-discs on both sides of the barrel. An overview of the vertex detector layout is given in Figure 3. The total area of the vertex detector is 0.53 m^2 .

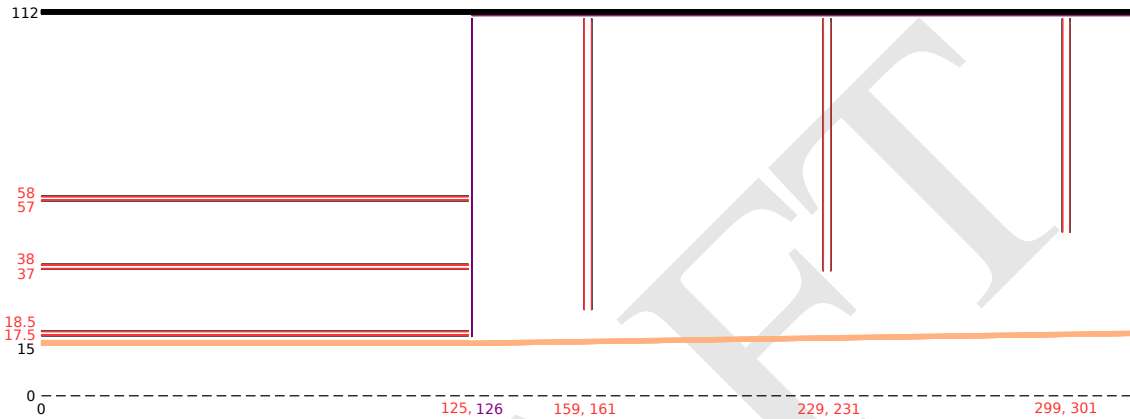


Figure 3: Sketch of the vertex detector barrel and forward region (in the ZR plane) of the CLD simulation model. Dimensions are given in mm. Red lines indicate sensors, black lines support structure, while magenta lines show cables. The vacuum pipe is shown in orange colour.

The vertex detector consists of $25 \times 25 \mu\text{m}^2$ pixels, with a silicon sensor thickness of $50 \mu\text{m}$. Using pulse height information and charge sharing, a single point resolution of $3 \mu\text{m}$ is aimed for.

The inner radius of the innermost vertex barrel layer is determined by the radius and thickness of the central beam pipe, which in turn is given by MDI constraints [4]. As a result, the inner edge of the innermost layer of the vertex barrel is located at $R = 17.5 \text{ mm}$. The location of the additional vertex barrel layers is obtained by scaling-down the layout of the CLICdet vertex detector layout.

The overall length of the barrel vertex detector, built from staves, is 250 mm . The double layer structure is shown in Figure 4. Further details on the dimensions of the vertex detector barrel layers used in the simulation model are given in Table 2. Note that the present numbers for the stave widths result from scaling-down the CLICdet layout - these are the numbers implemented in the simulation model. In a forthcoming engineering study, such layout details will have to be revised.

Table 2: Vertex barrel layout as implemented in the simulations.

Barrel layers	Inner radius [mm]	No. of staves	Stave width [mm]
1 - 2	17.5 - 18.8	16	7.3
3 - 4	37 - 38.3	12	20.2
5 - 6	57 - 58.3	16	23.1

The vertex detector forward region consists of three discs on each side, each disc is built as a double-layer device. The discs are located a distance from the IP of 160, 230 and 300 mm, respectively. They are constructed from 8 trapezoids, approximating a circle. For simplicity the trapezoids are not overlapping in the simulation model. The inner radii of the forward discs respects the 150 mrad cone reserved for

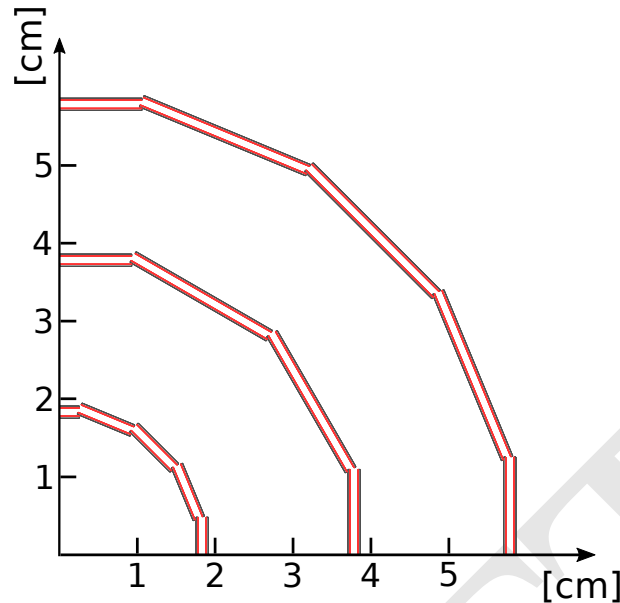


Figure 4: The double layer arrangement in the vertex barrel detector (XY view).

126 MDI elements. The dimensions of the vertex forward discs are given in Table 3. Contrary to CLICdet,
 127 the forward region vertex detector is built from planar discs, not from spirals as in CLICdet. An overview
 128 of the vertex petal arrangement as implemented in the simulation is shown in Figure 5.

Table 3: Dimensions of the vertex discs.

Vertex disc	Inner radius [mm]	Outer radius [mm]	Trapezoid inner edge [mm]	Trapezoid outer edge [mm]
1	24	102	19.9	84.5
2	34.5	102	28.6	84.5
3	45	102	37.3	84.5

129 3.2 Beam-Induced Backgrounds in the Vertex Detector Region

130 Beam-related backgrounds can potentially be significant drivers for the vertex (and tracker) technology
 131 choices and the requirements for the read-out of these detectors. Three types of backgrounds have been
 132 studied in detail: incoherent pair production and $\gamma\gamma \rightarrow$ hadrons production from beam-beam interactions,
 133 and background hits from synchrotron radiation. The studies using full Monte Carlo simulations and their
 134 results are described in detail in a dedicated chapter of the CDR [4]. Examples for incoherent pairs and
 135 synchrotron radiation at the lowest and highest energy of FCC-ee operation are given below. The rate of
 136 $\gamma\gamma \rightarrow$ hadrons events was found to be negligible (< 0.008 events per bunch crossing at 365 GeV, < 0.0007
 137 per bunch crossing at 91.2 GeV).

138 The simulations were performed using the latest version of the CLD detector model and applying a
 139 realistic field map (resulting from folding the detector main solenoid field and the fields of the compensating
 140 and screening solenoids). Figure 6 shows the resulting hit density from incoherent pairs per bunch
 141 crossing (BX) for operation at the Z-pole, at 91.2 GeV, while Figure 7 presents the same for the top
 142 energy, 365 GeV. At 91.2 GeV, the results are obtained from simulating 1806 bunch crossings, while at
 143 365 GeV sufficient statistical accuracy was obtained from 371 bunch crossings.

144 The corresponding results for hits related to synchrotron radiation photons (averaged over 10 bunch
 145 crossings) are shown in Figure 8. These hit rates are about a factor of five lower than the hits from

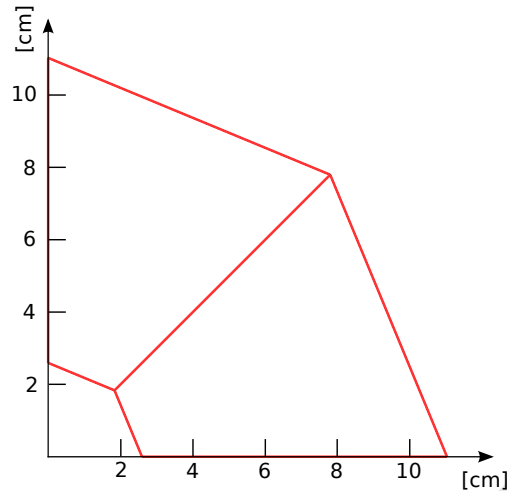


Figure 5: Schematic view of the first vertex forward disc, as implemented in the simulation model (XY view).

146 incoherent pairs. Note that there are no hits from synchrotron radiation observed at 91.2 GeV, even when
 147 accumulating data from more than 40000 bunch crossings.

148 From the hit densities obtained, one can deduce detector occupancies under certain assumptions, in
 149 analogy to what is described for CLICdet in [6].:

$$Occupancy/(readout\ window) = Hits/(mm^2 \cdot BX) \times n_{bunches}/(readout\ window) \times (1) \\ \times (pixel\ size) \times (avg.\ cluster\ size) \times (safety\ factor)$$

150 In the following, we are assuming a safety factor of 5 to account for uncertainties in the simulation,
 151 and charge sharing of 3 (which will depend on technology choices). In a scenario where the technology
 152 chosen for the ALICE ITS LS2 upgrade [7] is assumed, the readout time window would be 10 μ s. The
 153 present FCC-ee design parameters foresee a bunch spacing of 19.6 ns at 91.2 GeV, and of 3396 ns at
 154 365 GeV, leading to 510 and 3 bunch crossings, respectively, within the readout window. As a result,
 155 the estimated maximal occupancies per readout window (including the safety factor) are expected to be
 156 0.59% and 0.13% for operation at 91.2 and 365 GeV, respectively. It is expected that such occupancies
 157 from background hits are acceptable and will not, e.g., impact the performance of the pattern recognition
 158 algorithm of the tracking software.

159 3.3 Technology Choices, Cooling and Material Budget

160 The technologies available for vertex pixel sensors, readout electronics, mechanical support structures
 161 and cooling are rapidly evolving. At this stage of the conceptual design for CLD, the example of the
 162 ALICE ITS LS2 upgrade [7] is considered a good choice, or at least an acceptable approximation for the
 163 amount of material, to be used in the simulation model.

164 ALICE ITS upgrade uses very light-weight structures. The average power dissipation is measured in
 165 prototypes to be about 300 mW/cm^2 , and water cooling is used for the devices. Assuming this techno-
 166 logic, the total material budget per double layer in the CLD vertex detector is 0.6 % X_0 . For reference, this
 167 corresponds to 50% more material than in the CLICdet vertex detector (which assumes power pulsing
 168 and air cooling).

169 The low occupancies expected from incoherent pairs and synchrotron radiation (see section 3.2), at all
 170 energy stages of FCC-ee, allow to overlay events from a number of bunch crossings - this implies that

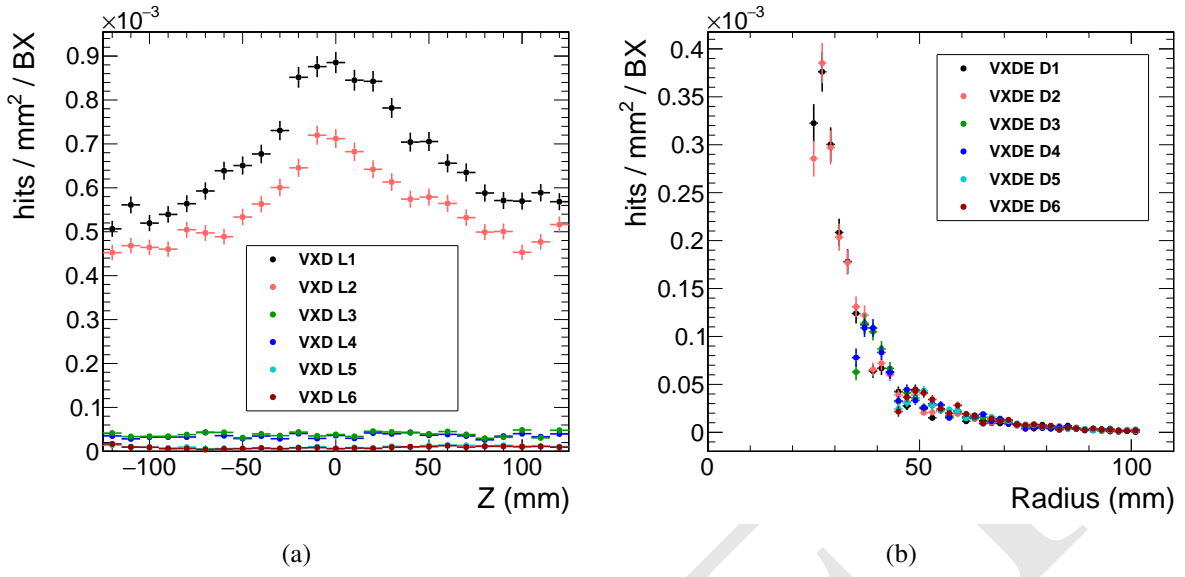


Figure 6: Hit densities per bunch crossing in the CLD vertex detector barrel layers (a) and discs (b) for particles originating from incoherent pairs. Results are shown for operation at 91.2 GeV. VXD L1-L6 indicates the vertex detector barrel layers, while VXDE D1-D6 stands for the vertex detector forward discs. Vertical error bars indicate the statistical uncertainty, horizontal bars are drawn to show the bin size. Safety factors for the simulation uncertainties are not included.

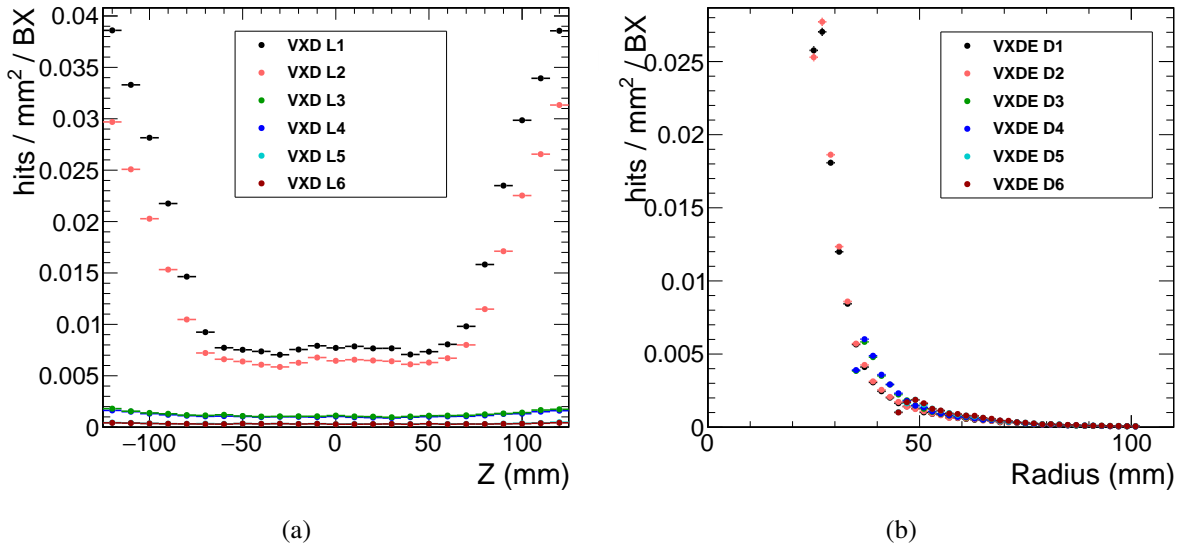


Figure 7: Hit densities per bunch crossing in the CLD vertex detector barrel layers (a) and discs (b) for particles originating from incoherent pairs, for operation at 365 GeV. Vertical error bars indicate the statistical uncertainty, horizontal bars are drawn to show the bin size. Safety factors for the simulation uncertainties are not included.

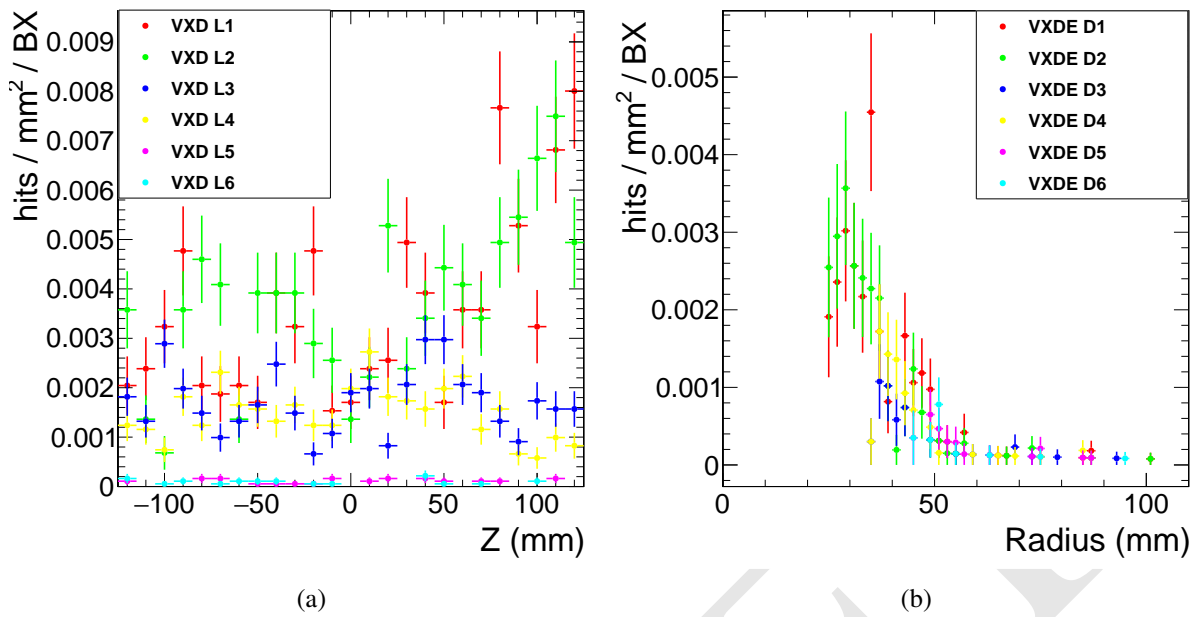


Figure 8: As Figure 7 but for hits related to synchrotron radiation photons.

171 rather modest readout times are acceptable for the CLD vertex detector.

172 A simplified vertex layer layout is implemented in the simulation model. The $50\ \mu\text{m}$ silicon sensors are
 173 separated by a 1 mm air-gap in the barrel and a 2 mm air-gap in the discs. On the outside of each sensor,
 174 additional material represented by $235\ \mu\text{m}$ of silicon replaces the combined material of ASIC, support
 175 structure, connectivity and cooling. The resulting total material budget per double layer corresponds to
 176 the thickness in X_0 expected to emerge from the engineering design (and has been achieved in ALICE
 177 ITS upgrade). A summary is given in Table 4. Note that, in analogy to CLICdet, slightly more material
 178 is assumed to be needed for the mechanical support of the vertex discs w.r.t. the barrel layers, resulting
 179 in a total material budget of $0.7\ \% X_0$ for the discs.

Table 4: Vertex detector double layer material budget as implemented in the simulations.

Function	Material	Barrel		Discs	
		Thickness [μm]	Material budget [% X_0]	Thickness [μm]	Material budget [% X_0]
ASIC, support etc.	Silicon	235	0.259	280	0.298
Sensor	Silicon	50	0.053	50	0.053
Gap	Air	1000	0.001	2000	0.001
Sensor	Silicon	50	0.053	50	0.053
ASIC, support etc.	Silicon	235	0.259	280	0.298
total		0.625		0.703	

4 Tracking System

4.1 Overview and Layout

In analogy to CLICdet, the CLD concept features an all-silicon tracker. Engineering and maintenance considerations led to the concept of a main support tube for the inner tracker region (including the vertex detector). The inner tracker consists of three barrel layers and seven forward discs. The outer tracker completes the system with an additional three barrel layers and four discs. The overall layout of the silicon tracker in CLD is shown in Figure 9.

The tracking volume has a half-length of 2.2 m and an maximum radius of 2.1 m. This radius allows to achieve, approximately, the same momentum resolution in the CLD tracking system with a 2 T magnetic field as in the CLICdet tracker with a 4 T field and a radius of 1.5 m. The main support tube has an inner and outer radius of 0.686 and 0.690 m, respectively, and a half-length of 2.3 m. The layout respects the 150 mrad cone reserved for beam- and MDI-equipment. The overall geometrical parameters of the tracker are given in Table 5 and 6 for the barrel and discs, respectively.

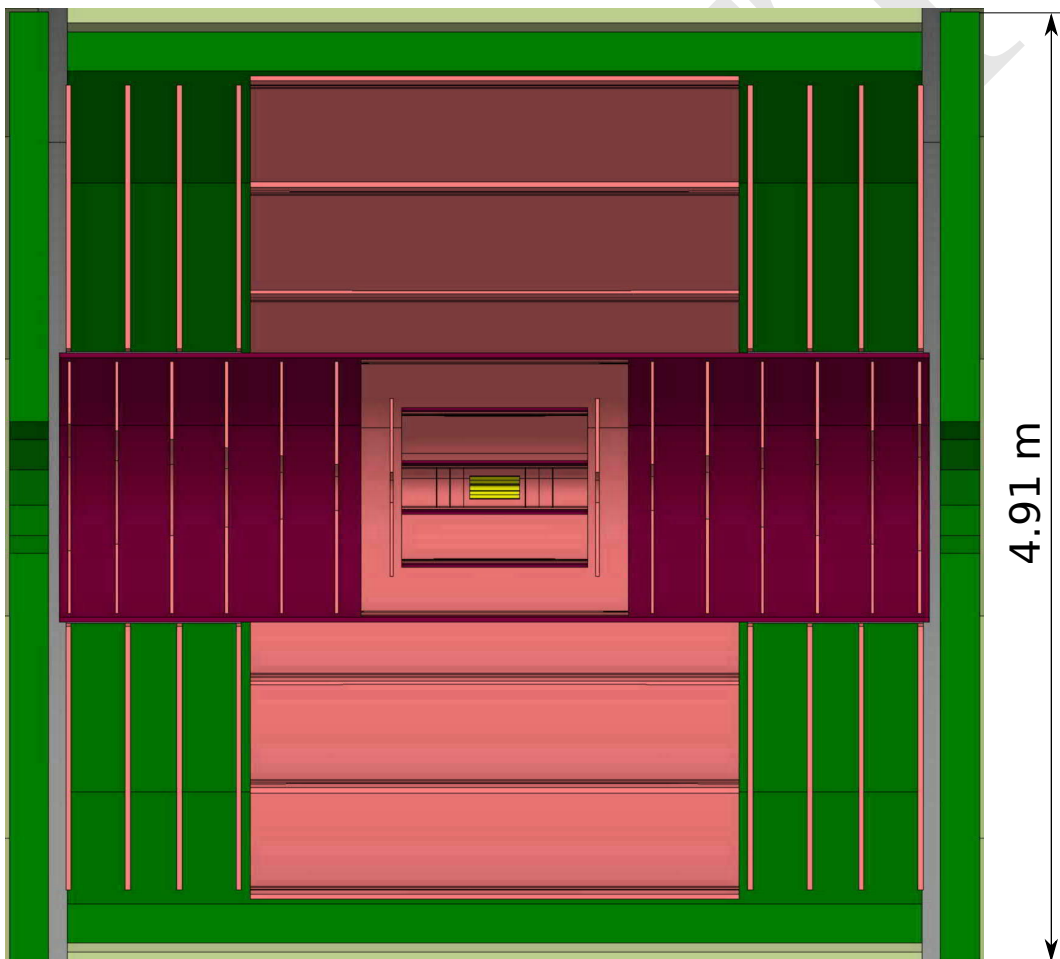


Figure 9: Overall layout of the CLD tracking system: the area in darker red illustrates the main support tube for the inner tracking region and the vertex detector. The tracking system covers polar angles larger than 150 mrad.

The pixel vertex detector and the silicon tracker are treated as one unified tracking system in simulation and reconstruction. The number of expected hits in CLD as a function of polar angle θ is shown in Figure 10.

Table 5: Main parameters of the tracker barrel layout, radius R and half-length L/2.

Layer No.	Name	R [mm]	L/2 [mm]
1	ITB1	127	482
2	ITB2	400	482
3	ITB3	670	692
4	OTB1	1000	1264
5	OTB2	1568	1264
6	OTB3	2136	1264

Table 6: Main parameters of the tracker discs.

Disc No.	Name	Z [mm]	R_{in} [mm]	R_{out} [mm]
1	ITD1	524	79.5	457
2	ITD2	808	123.5	652
3	ITD3	1093	165	663
4	ITD4	1377	207.5	660.5
5	ITD5	1661	249.5	657
6	ITD6	1946	293	640
7	ITD7	2190	330	647
8	OTD1	1310	718	2080
9	OTD2	1617	718	2080
10	OTD3	1883	718	2080
11	OTD4	2190	718	2080

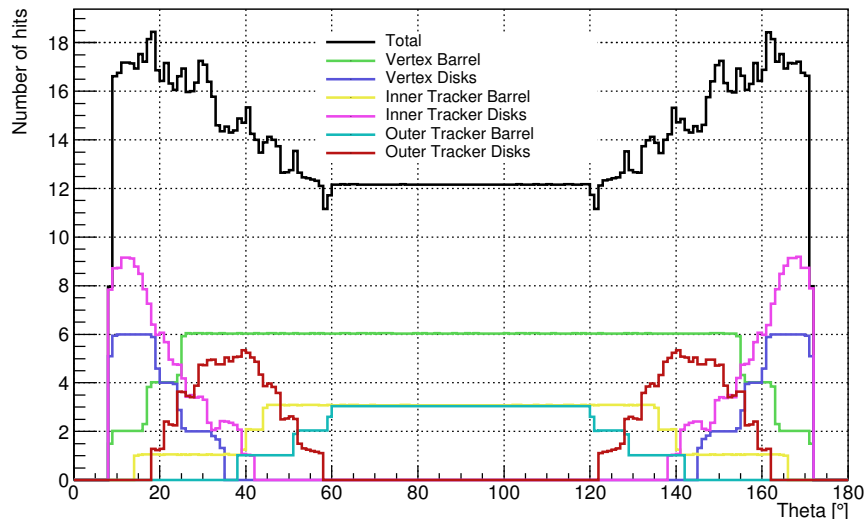


Figure 10: The coverage of the tracking systems as a function of the polar angle θ . Shown is the mean number of hits (averaged over ϕ) created by Geantino¹ in full simulation. At least eight hits are measured for all tracks with a polar angle down to $8^\circ 33'$.

196 Preliminary engineering studies have been performed for CLICdet to define the support structures,
 197 cooling systems etc. needed for the tracker barrel layers and discs. For the outer tracker barrel support,
 198 these studies were completed by building and testing a prototype [8]. At the present level of a conceptual
 199 design, the same concepts and material thicknesses are used for CLD. The material budget needed in
 200 addition to the 200 μm thick layer of silicon (sensors plus ASICs or monolithic structure) is estimated.
 201 In addition to the cylindrical main support tube, two carbon fibre structures ("interlink structures") are
 202 needed, to mount the inner and outer tracker barrel layers and to route connections. Very preliminary
 203 sketches of these two interlink structures exist [9].

204 The building blocks from which the tracker detection layers are constructed, are modules of sensor plus
 205 ASIC. They are glued on one side to multi-layer carbon fiber structures acting as supports and containing

¹Geantino is an artificial particle from GEANT4 which is used as a geometrical probe.

Table 7: Material budget of the tracker barrel layers - total per barrel layer, as implemented in the simulation.

Layer Name	X_0 [%]
ITB1 - 3	1.09
OTB1	1.28
OTB2 - 3	1.15

Table 8: Material budget of the tracker discs - total per disc, as implemented in the simulation.

Disc Name	X_0 [%]
ITD1	1.34 - 1.87
ITD2	1.28 - 2.13
ITD3	1.39 - 2.03
ITD4	1.39 - 1.76
ITD5	1.39 - 1.79
ITD6	1.41 - 1.75
ITD7	1.34 - 1.68
OTD1 - 4	1.37 - 1.91

the cooling. On the other side, these modules are glued to the elements needed for connectivity. In the tracker discs, modules are arranged into petals, which in turn are assembled into the full discs. In the inner and outer barrel, the silicon sensor size for all modules is $30 \times 30 \text{ mm}^2$. In the present simulation model, in the barrel an overlap between modules of 0.1 mm is implemented in azimuthal direction - there is no overlap along the detector axis. The outer tracker discs are assembled from the same type of modules, $30 \times 30 \text{ mm}^2$, while the inner tracker discs are made of modules with $15 \times 15 \text{ mm}^2$ sensors. In all tracker discs, a considerable overlap between petals is foreseen while modules inside the petals have no overlap. Details of the present ideas on module support, overlaps etc. can be found in [9] for the case of CLICdet - the same design principles are followed for CLD.

This preliminary engineering model is implemented in the simulation model of the tracker, with emphasis on the correct total material budget per layer (in X_0). The current implementation is shown in Figures 11 and 12. Simplifications with respect to the engineering model include the use of larger rectangular surfaces instead of the small modules in the tracker disc petals, as shown in Figure 13.

The total material budget for the different tracker layers is listed in Tables 7 and 8. The material budget for the modules (sensor and electronics) plus cooling and connectivity, is estimated to be 1.09% X_0 per layer for ITB's and 1.15-1.28% X_0 for OTB's. This material budget does not include the tracker support structures, made of carbon fibre components, which differ from layer to layer and amount to 0.13% X_0 to 0.37% X_0 per layer. The CLD simulation model includes this additional material.

Details on the different contributions to the total material budget can be found in [9]. In the CLD simulation model, the inner and outer interlink structures are inserted with 0.6% X_0 , approximately accounting for the actual graphite structure plus some of the cables. An additional support structure, for the vertex barrel layers and discs, is also inserted with 0.6% X_0 . The main support tube, in its preliminary design, amounts to 1.25% X_0 . The total material budget for the vertex plus tracker region as a function of polar angle is shown in Figure 14.

4.2 Beam-Induced Backgrounds in the Tracking Region

The results of full detector simulation studies showing background hits from incoherent pairs in the tracker region are given in Figures 15 for operation at the Z, 91.2 GeV. Note that at this beam energy, no hits are observed originating from synchrotron radiation photons. The results for 365 GeV are given in Figures 16 (for pairs) and 17 (for synchrotron radiation). From these hit densities, in analogy to section 3.2, the expected peak occupancies can be obtained. Similarly to CLICdet, for the CLD tracker we assume that small strip or pixel detectors with a maximum cell size of $50 \text{ }\mu\text{m}$ width and 1 mm length will be used throughout. In a technical design phase, the layout details will have to be refined. Assuming

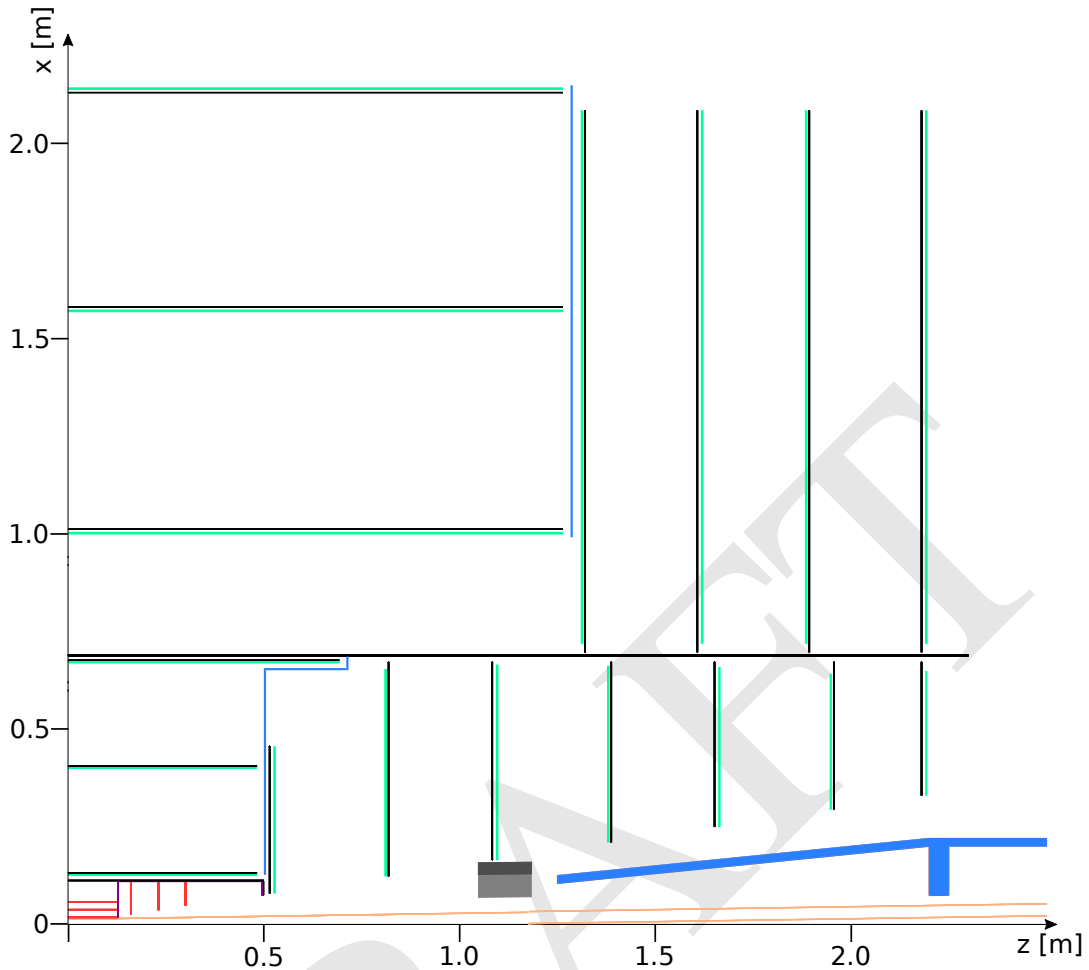


Figure 11: XZ-view of the tracker as implemented in the simulation model. The black lines indicate the tracker support structures including cooling and cables, and the main support tube. The green lines represent the tracker sensor layers. The blue lines show the carbon-fibre interlink structures. The vertex detector is shown in the centre (in red). Cables going outwards from the vertex detector are represented in magenta. The LumiCal is represented by the small grey box near $z = 1.2$ m. The conical and cylindrical structures (in blue) downstream of LumiCal represent material (steel) in place of the compensating and shielding solenoids. Also indicated is the vacuum tube (in orange).

238 a cluster size of 3, a safety factor of 5 and a readout window of $10 \mu\text{s}$, the occupancy at 91.2 GeV
 239 operation will be less than 1%. For the same assumptions, the occupancy at 365 GeV (from pairs and
 240 synchrotron radiation combined) is expected to be below 0.15%.

241 Note that the highest occupancies in the tracker detectors are found in a rather small region of the first
 242 two inner tracker discs. Similarly to what is described for CLICdet in [6], to further reduce the occupancy
 243 these regions can be equipped with smaller strips or replaced by pixel detectors.

244 4.3 Technology Choices and Cooling

245 The ALICE ITS upgrade outer tracker technology [7] appears to be a suitable choice for the CLD tracker.
 246 The integration time window of the chip of $10 \mu\text{s}$ does not appear to give rise to too high occupancies,
 247 and the power dissipation of 130 mW/cm^2 is low (100 mW/cm^2 for the chips plus 30% for the power
 248 regulators). A leak-less de-mineralized water cooling system is used. The average material budget in the

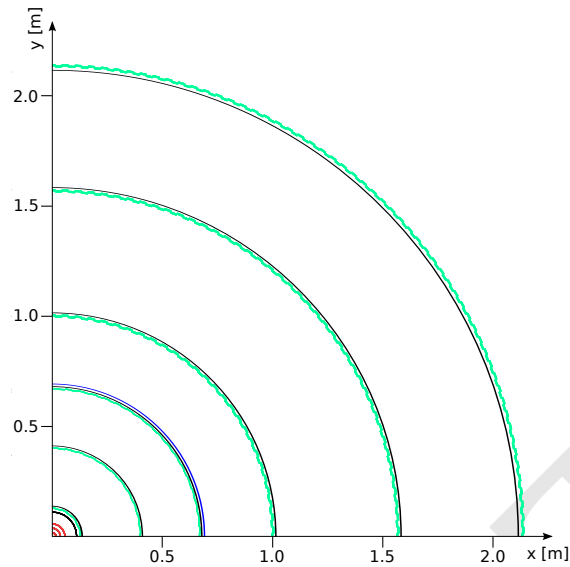


Figure 12: XY-view of the tracker barrel layers as implemented in the simulation model. The black lines indicate the support structures including cooling and cables, the green lines represent the tracker sensor layers. The blue line shows the main support tube. The vertex detector (in red) is shown in the centre.

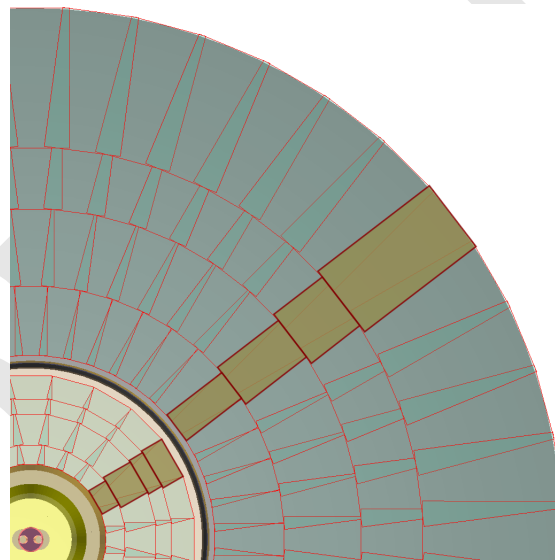


Figure 13: XY-illustration of the tracker disc implementation in the simulation model: the overlap between petals is visible as darker, smaller wedges. The petals are constructed from three (or four) rectangular volumes (example highlighted in yellow/brown), a simplification with respect to the engineering layout in [9]. This graph is a view from $z = 1800$ mm in downstream direction, thus showing the ITD6 and OTD3 inner and outer tracker discs.

249 ALICE ITS outer tracker is $0.8\% X_0$ per layer, with twelve peaks of 1.2% and $1.4\% X_0$ in the azimuthal
 250 distribution. The material budget assumed for the CLD tracking detector layers, which varies from 1 to
 251 $2\% X_0$, seems adequate at this stage.

252 Since the surface area in CLD (195 m^2) is much larger than the one of the ALICE ITS upgrade (9.4
 253 m^2), a number of engineering issues will have to be investigated. Not least, the total heat load in the

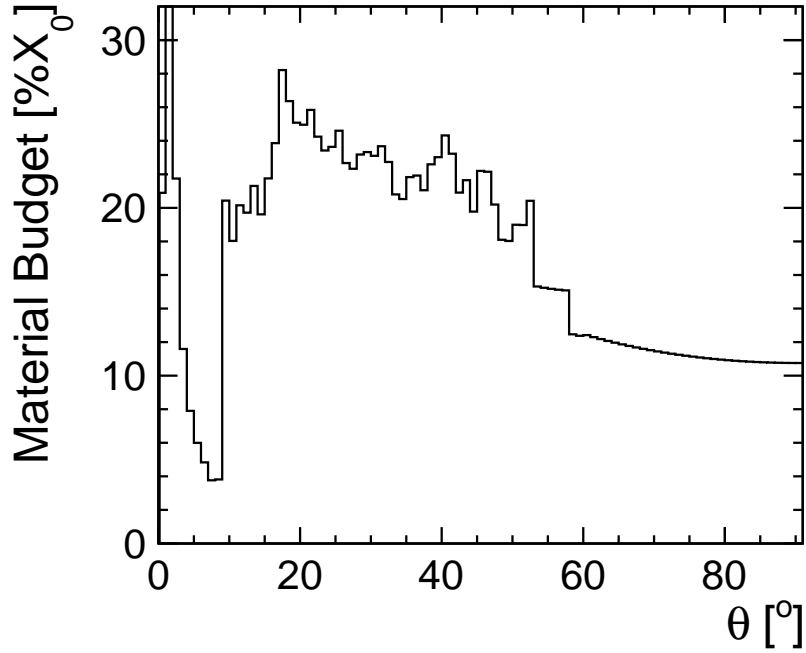


Figure 14: Total material budget of the vertex plus tracker system in CLD, including beam pipe, supports and cables, as a function of the polar angle (averaged over ϕ) - as implemented in the simulation model.

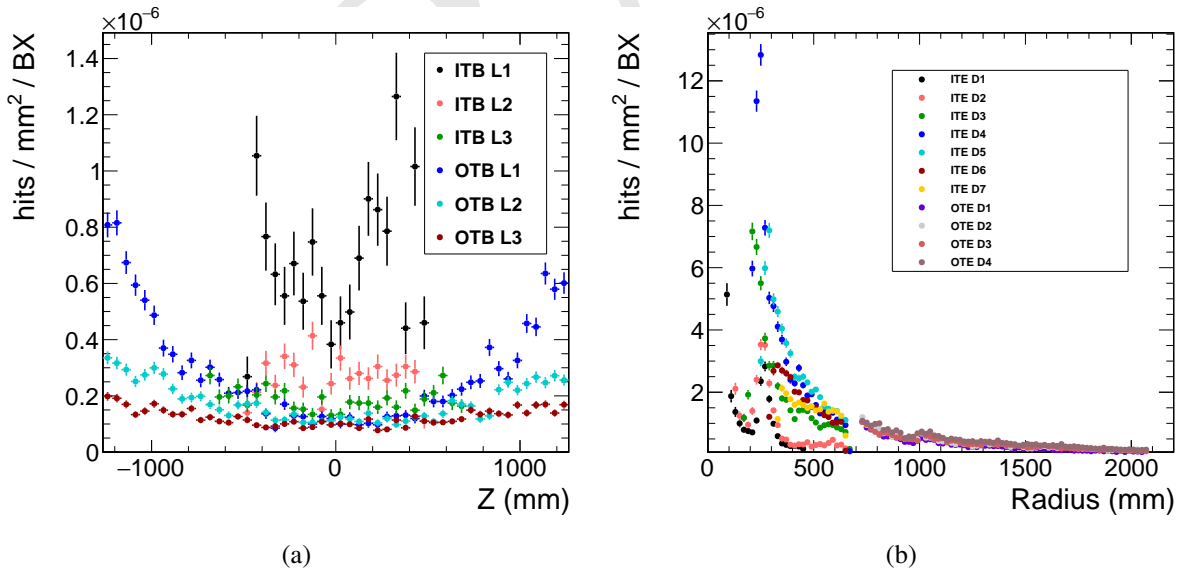


Figure 15: Hit densities in the CLD tracking detector barrel layers (a) and discs (b) for particles originating from incoherent pairs. Results are shown for operation at 91.2 GeV ITB and OTB stand for inner and outer tracker barrel layers, ITE and OTE for inner and outer tracker forward discs, respectively. Vertical error bars show the statistical uncertainty, horizontal bars indicate the bin size. Safety factors for the simulation uncertainties are not included.

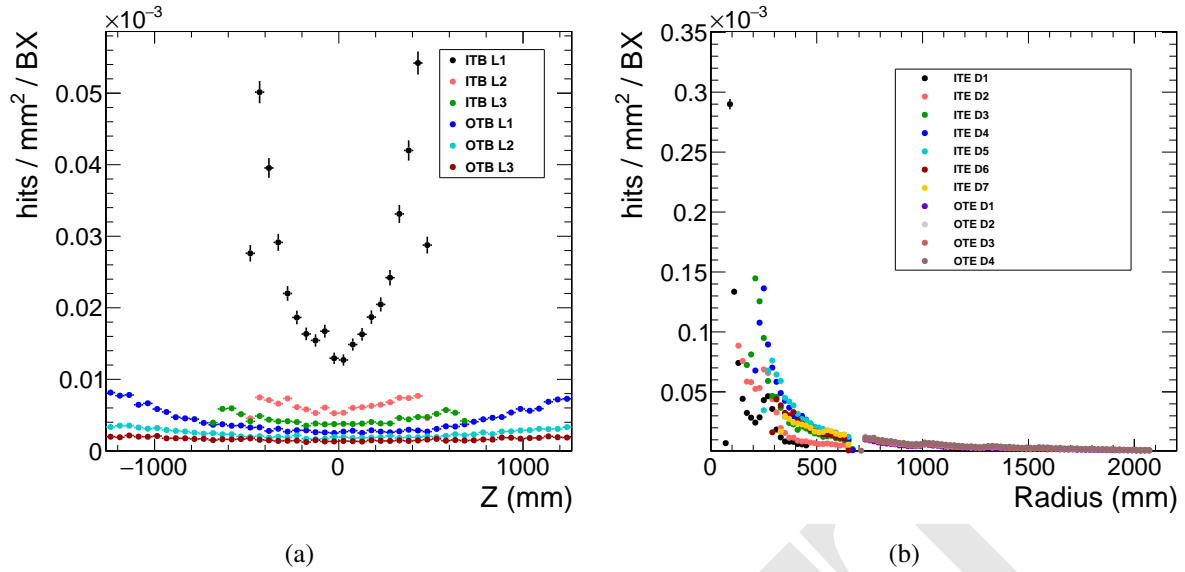


Figure 16: Hit densities in the CLD tracking detector barrel layers (a) and discs (b) for particles originating from incoherent pairs, for operation at 365 GeV. Vertical error bars show the statistical uncertainty, horizontal bars indicate the bin size. Safety factors for the simulation uncertainties are not included.

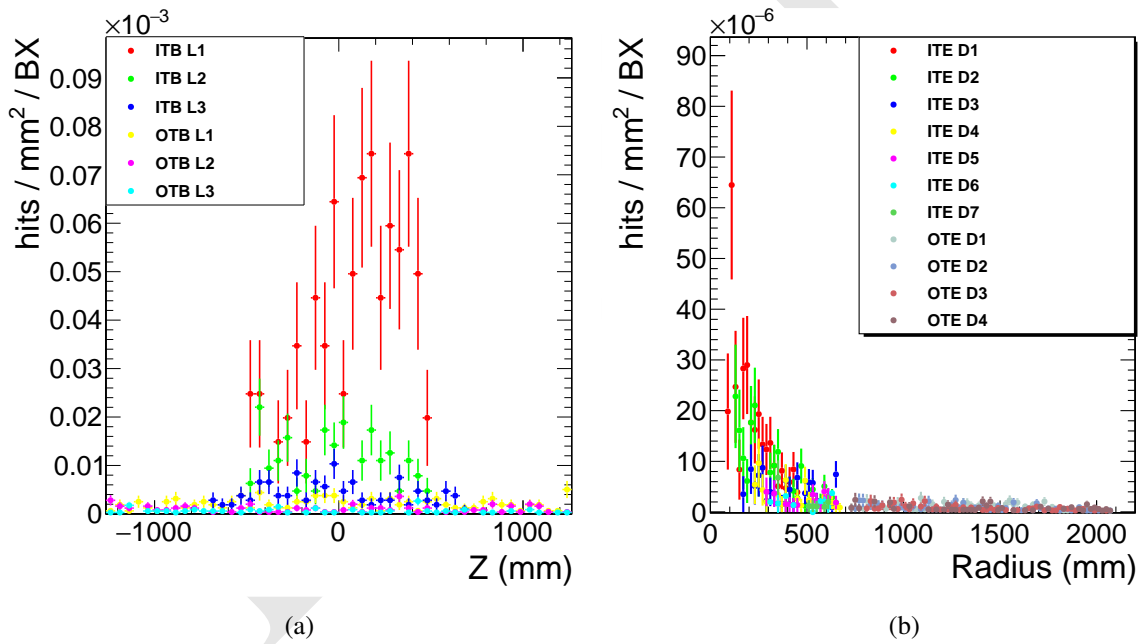


Figure 17: As Figure 16 but for hits related to synchrotron radiation photons.

254 tracker will be around 180 kW and an adequate cooling infrastructure to reach the tracker elements,
 255 which are distributed over a large volume, will be needed.

5 Calorimetry

5.1 Introduction

Extensive studies in the context of ILC and CLIC have revealed that high granularity particle flow calorimetry appears to be a promising option to reach the required jet energy resolution of 3-4 %. Such a performance is necessary to allow the distinction e.g. of W and Z bosons on an event-by-event basis.

In contrast to a purely calorimetric measurement, particle flow calorimetry requires the reconstruction of the four-vectors of all visible particles in an event. The momenta of charged particles (about 60% of the jet energy) are measured in the tracking detectors. Photons (about 30% of the jet energy) and neutral hadrons are measured in the electromagnetic and hadronic calorimeter, respectively. An overview of particle flow and the PandoraPFA software can be found in [10–12]. Experimental tests of particle flow calorimetry are described in detail in [13]. A recent presentation provides updates on results obtained by the CALICE collaboration [14].

5.2 Electromagnetic Calorimeter

The segmentation of the ECAL has to be sufficient to resolve energy depositions from near by particles in high energy jets. Studies performed in the context of the ILC and CLIC suggest a calorimeter transverse segmentation of $5 \times 5 \text{ mm}^2$. The technology chosen as baseline option for the detectors at the linear colliders is a silicon-tungsten sandwich structure. In order to limit the leakage beyond the ECAL, a total depth of around 22-23 X_0 is chosen.

In order to investigate the ECAL performance for different longitudinal sampling options, a series of full simulation studies was performed for the CLICdet study [1]. As a result, a longitudinal segmentation with 40 identical Si-W layers (using 1.9 mm thick W plates) was found to give the best photon energy resolution over a wide energy range. This detector design is also implemented in the CLD simulation model.

The overall dimensions of the ECAL are given in Table 9. The detailed ECAL segmentation as implemented in the simulation model is shown in Figure 18 and is given in Table 10. A distance of 3.15 mm between W plates is chosen to accommodate sensors and readout, in analogy to CLICdet and ILD at ILC. Note that the ECAL starts with an absorber layer, followed by a sensor/electronics layer, and so on. The last element in the ECAL stack is a sensor/electronics layer. A section of the ECAL barrel as implemented in the simulations is shown in Figure 19.

Table 9: ECAL layouts implemented in the simulation model (dimensions in mm).

ECAL barrel r_{\min}	2150
ECAL barrel r_{\max}	2352
ECAL barrel z_{\max}	2210
ECAL endcap z_{\min}	2307
ECAL endcap z_{\max}	2509
ECAL endcap r_{\min}	340
ECAL endcap r_{\max}	2455

Table 10: Parameters for the ECAL segmentation as implemented in the simulation model, with a total of 40 SiW layers.

Function	Material	Layer thickness [mm]
absorber	tungsten alloy	1.90
Insulator	G10	0.15
Connectivity	mixed (86% Cu)	0.10
Sensor	silicon	0.50
Space	air	0.10
PCB	mixed (82% Cu)	1.30
Space	air	0.25
Insulator	G10	0.75
Total between W plates		3.15
Total SiW layer		5.05

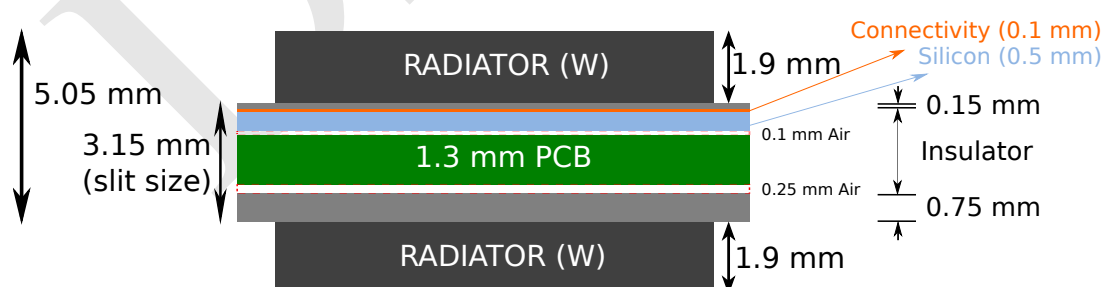


Figure 18: Schematic drawing of the ECAL segmentation as implemented in the simulation model.

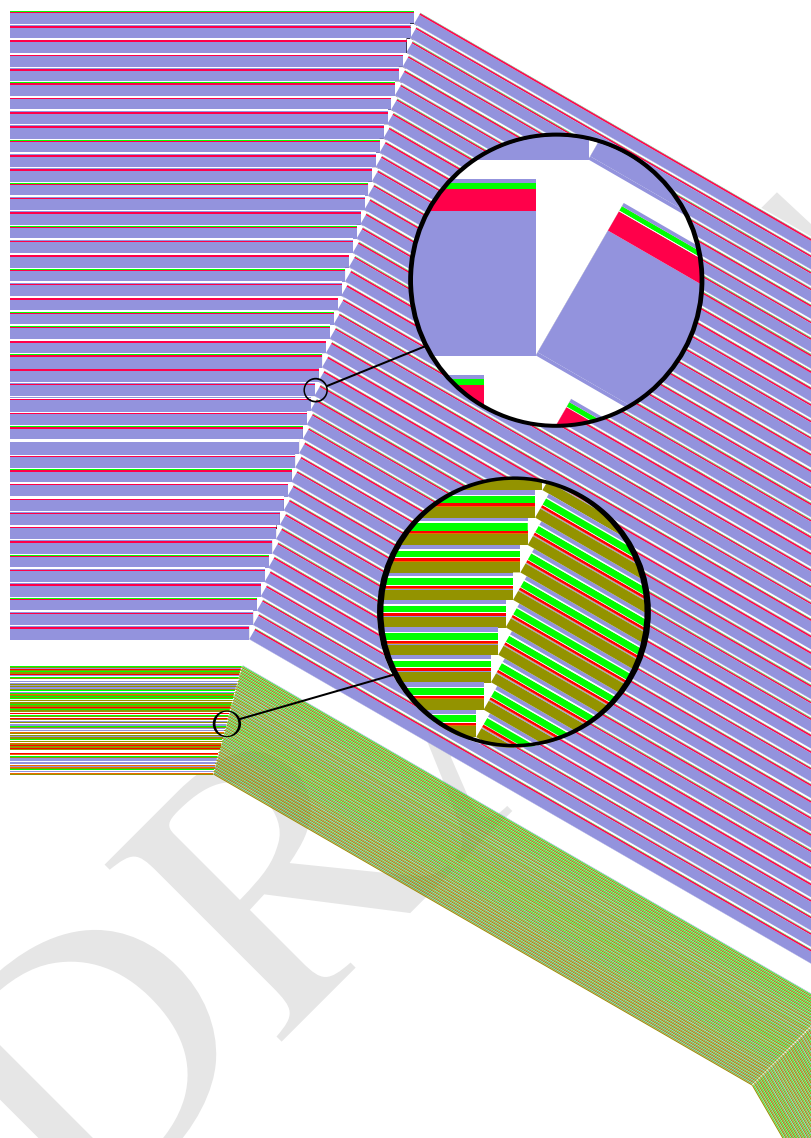


Figure 19: Implementation of ECAL and HCAL in the simulation model (the reader may need to zoom in to see all the details). The region of a junction between two sectors (of the dodecagon) in the barrel region is shown. In the ECAL, the olive-green regions indicate the tungsten layers, while the red regions symbolize the silicon sensors. Purple layers are G10 insulator, green is PCB and connectivity, and white is air. In the HCAL, blue regions indicate the steel layers (with thin steel sheets for the cassette), red stands for the scintillator, while green and white are PCB and air as in the ECAL.

285 5.3 Hadronic Calorimeter

286 Detailed optimisation studies have been performed for the HCAL foreseen in the detectors at ILC and
 287 CLIC. Details of recent studies for CLICdet are described in [15].

288 The proposed hadronic calorimeter of CLD has a structure and granularity as the one in CLICdet. It
 289 consists of steel absorber plates, each of them 19 mm thick, interleaved with scintillator tiles, similar to
 290 the CALICE calorimeter design for the ILD detector at ILC [16]. The gap for the sensitive layers and
 291 their cassette is 7.5 mm. The polystyrene scintillator in the cassette is 3 mm thick with a tile size of
 292 $30 \times 30 \text{ mm}^2$. Analog readout of the tiles with SiPMs is envisaged. The HCAL consists of 44 layers
 293 and thus is around $5.5 \lambda_I$ deep, which brings the combined thickness of ECAL and HCAL to $6.5 \lambda_I$ (see
 294 Figure 20). In the studies performed for the ILD detector at ILC (500 GeV), this depth of the calorimetry
 295 for hadrons was found to be sufficient. The overall dimensions of the HCAL are summarized in Table 11.
 296 In the simulations, the part of the HCAL endcap which surrounds the ECAL endcap (see Figure 1) is
 297 treated as a separate entity called the "HCAL ring". The detailed HCAL segmentation as implemented
 298 in the simulation model is shown in Figure 21 and is given in Table 12.

299 A section of the HCAL barrel as implemented in the simulations is shown in Figure 19.

Table 11: HCAL overall layout as implemented in the simulation model (dimensions in mm).

HCAL barrel r_{\min}	2400
HCAL barrel r_{\max}	3566
HCAL barrel z_{\max}	2210
HCAL endcap z_{\min}	2539
HCAL endcap z_{\max}	3705
HCAL endcap r_{\min}	340
HCAL endcap r_{\max}	3566
HCAL ring z_{\min}	2353.5
HCAL ring z_{\max}	2539
HCAL ring r_{\min}	2475
HCAL ring r_{\max}	3566

Table 12: Parameters for the HCAL segmentation as implemented in the simulation model, with a total of 44 Fe-Scintillator layers.

Function	Material	Layer thickness [mm]
Absorber	steel	19
Space	air	2.7
Cassette	Steel	0.5
PCB	mixed	0.7
Conductor	Cu	0.1
Scintillator	Polystyrene	3
Cassette	Steel	0.5
Total between steel plates		7.5
Total Fe-scint. layer		26.5

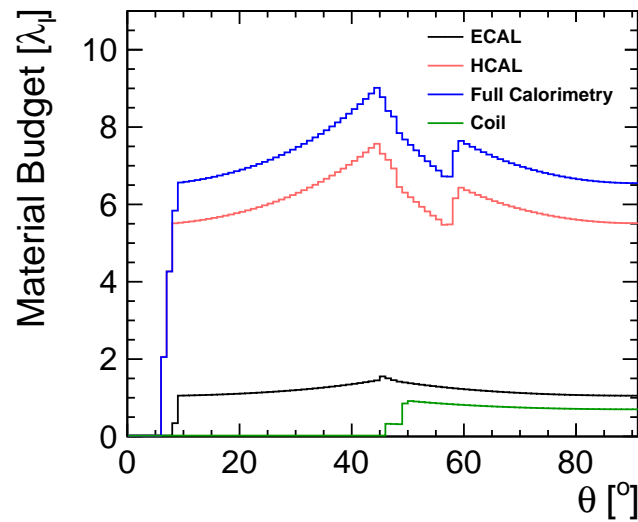


Figure 20: Nuclear interaction lengths λ_I in the calorimeters as a function of the polar angle θ . The interaction length corresponding to the material of the superconducting coil is shown for completeness.

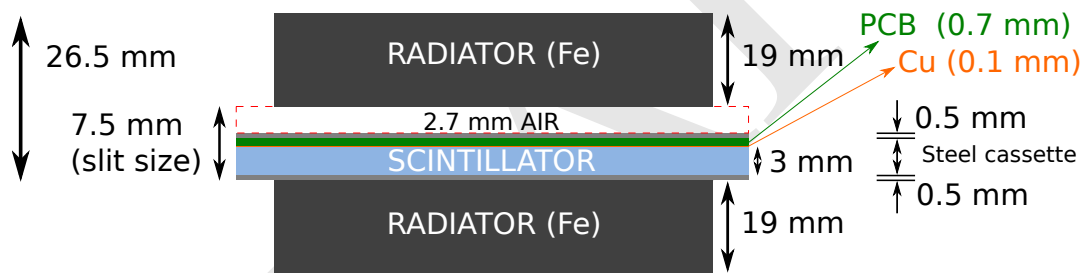


Figure 21: Schematic drawing of HCAL segmentation as implemented in the simulation model.

300 5.4 Technology Choices and Cooling

301 Presently, the technology assumed for the simulation model of the CLD ECAL silicon-tungsten sampling
 302 calorimeter is identical to the solution pursued by ILD/CALICE. In this layout, a thin copper sheet in contact
 303 with the distributed ASICs (via a thermally conducting grease) allows to remove the heat. A leak-less
 304 water cooling system is foreseen to be connected at the outer end of each module [17], [18], [19], [20].
 305 Thanks to power pulsing, the total heat load from the 77 million channels of the ECAL (barrel plus
 306 endcaps) is only 4.6 kW.

307 Without power pulsing and using the same technology a heat load 50 to 100 times higher is expected.
 308 This will impose the use of a different cooling scheme, and might ultimately lead to a different ECAL
 309 design - possibly inspired by the solution chosen for the CMS HGCAL project [21].

310 The ILD/CALICE technology has also been assumed for the CLD HCAL simulation model. The steel
 311 absorber plates in this calorimeter are 19 mm thick. Cooling as foreseen in ILD consists of conducting the
 312 heat to the edges of the modules using these steel plates, where water cooling manifolds are connected
 313 to them. In the technology chosen for the ILD HCAL, and using power pulsing, the average power
 314 dissipated is found to be 40 μ W per channel.

315 CALICE prototype layers with 4×144 channels have operated continuously (no power pulsing) and
 316 a preliminary version of the cooling system has been tested successfully. Such a number of channels
 317 operated continuously corresponds to the heat dissipation of a fully equipped ILD layer with power

318 pulsing.

319 For the HCAL of CLD, with much higher power dissipation, the cooling system will have to be
320 redesigned. Modifying the absorber layers by adding copper plates might be a solution. This will lead to
321 a different longitudinal sampling in the HCAL and will impact the performance of the calorimeter.

322 Detailed engineering studies and further simulations will be needed to assess the different design
323 options for ECAL and HCAL - this type of work goes beyond the present CDR scope.

DRAFT

6 Magnet System

6.1 Superconducting Solenoid

The solenoid magnetic field of the FCC-ee detectors is 2 T, which is limited by MDI constraints. Design details of the superconducting solenoid are described in [22].

In the simulation model, the magnetic field in CLD is 2 T throughout the volume inside the superconducting coil. The field in the yoke barrel is 1 T, pointing in the opposite direction with respect to the inner field. The simulation model currently assumes no field in the yoke endcap nor outside the yoke.

The solenoid of CLD is implemented in the simulation model with parameters as shown in Table 13. The material budget of the solenoid corresponds to about $0.7 \lambda_1$, as indicated in Figure 20.

Table 13: Description of the coil elements as implemented in the simulation model. For all elements the material, the longitudinal extent in one half of the detector $z_{\min/\max}$ and the radial extent $r_{\min/\max}$ are given.

Element	Material	z_{\min} [mm]	z_{\max} [mm]	r_{\min} [mm]	r_{\max} [mm]
Inner Barrel	Steel	0	3705	3719	3759
Coil	Aluminium	0	3467	3885	3975
Outer Barrel	Steel	0	3705	4232	4272
End plates	Steel	3665	3705	3759	4232

6.2 Yoke and Muon Detectors

The iron return yoke is structured into three rings in the barrel region and the two endcaps, as shown in Figure 22. The thickness of the yoke is reduced w.r.t. CLICdet, in correspondance to the lower solenoid field (2 T vs. 4 T).

A muon system, aimed at muon identification, with 6 layers as in CLICdet is implemented. An additional 7th layer is inserted in the barrel as close as possible to the coil. This layer may serve as tail catcher for hadron showers. The muon system layout in CLD is shown in Figure 23.

The muon detection layers are proposed to be built as RPCs with cells of $30 \times 30 \text{ mm}^2$ (alternatively, crossed scintillator bars could be envisaged). The free space between yoke steel layers is 40 mm, which is considered generous given present-day technologies for building RPCs. In analogy to CMS and CLICdet, the yoke layers and thus the muon detectors are staggered to avoid gaps (see Figure 2).

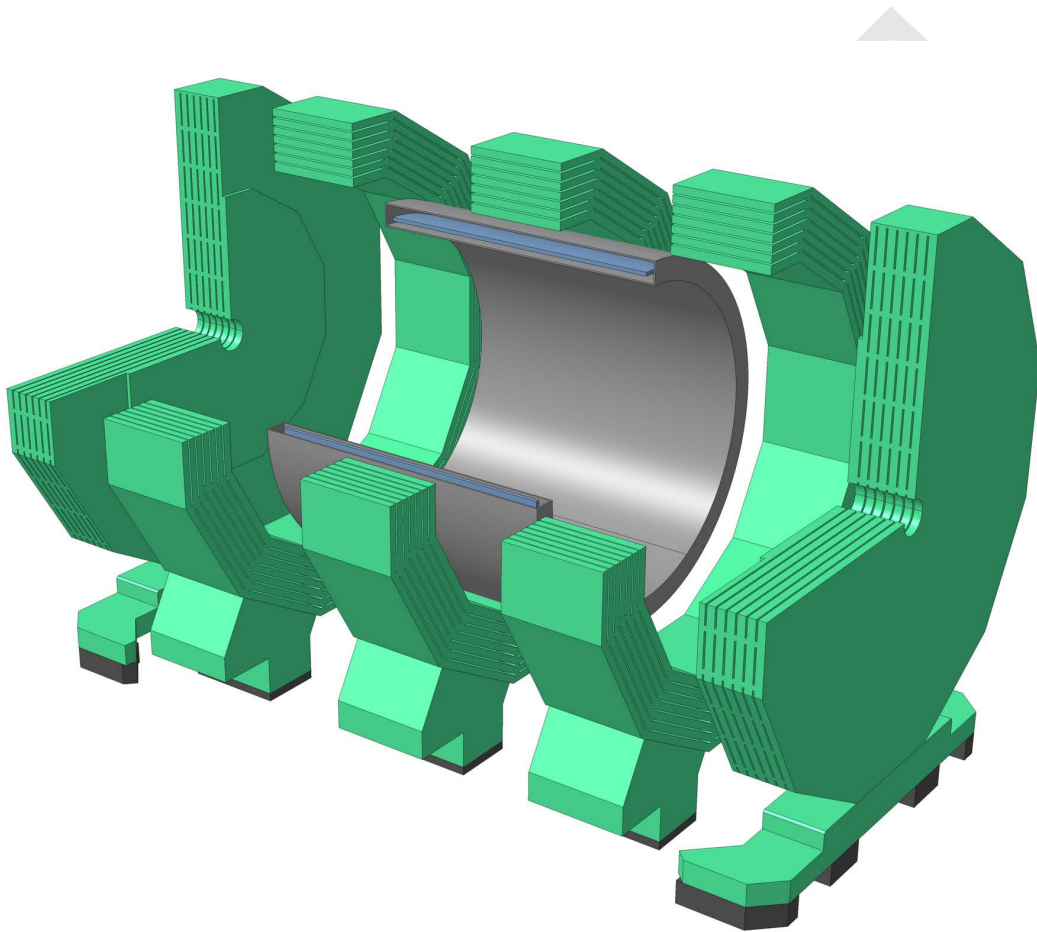


Figure 22: Segmentation of the iron return yoke of CLD into endcaps and three barrel rings.

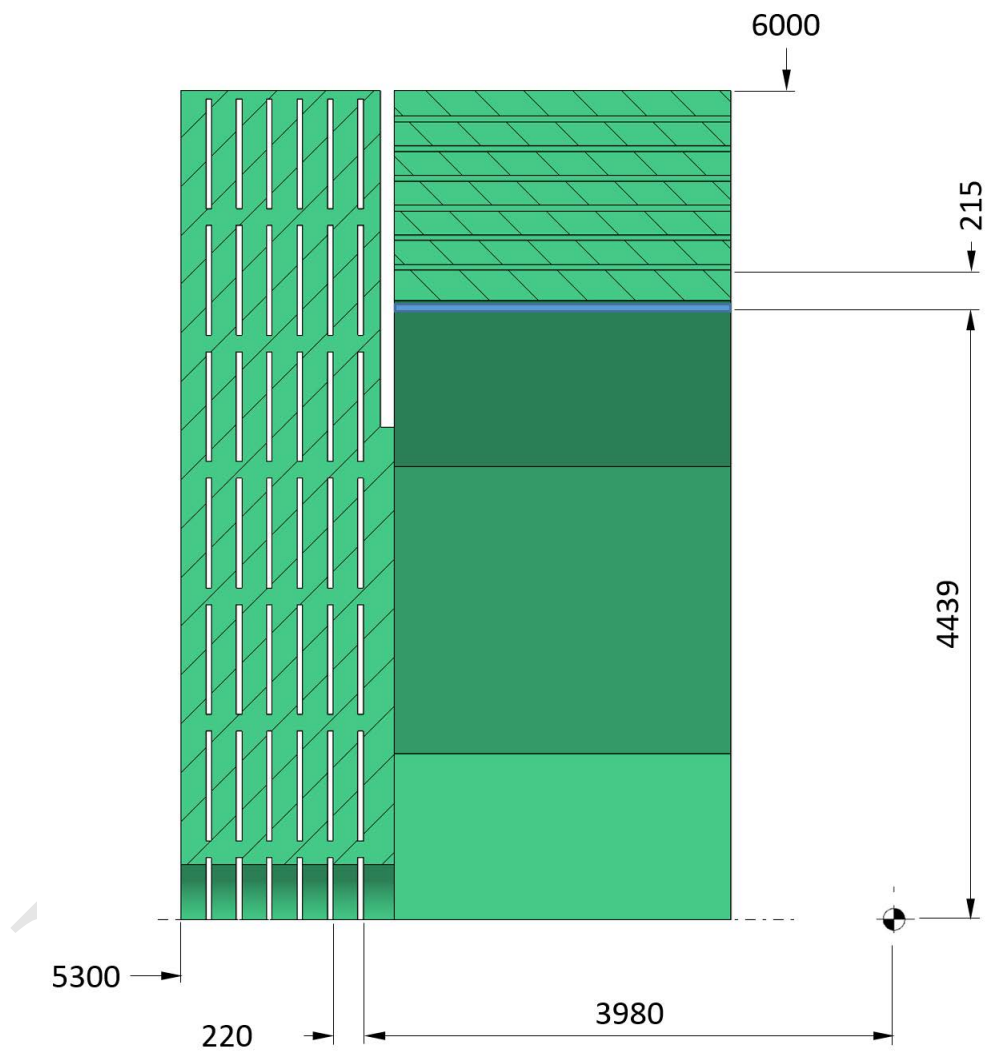


Figure 23: Schematic cross section of the muon system layout in the yoke of CLD. The staggering of the layers is not visible in this cross section.

7 Physics Performance

7.1 Simulation and Reconstruction

The detector simulation and reconstruction software tools used for the results presented in the following are developed together with the linear collider community. The DD4HEP [23] detector simulation and geometry framework was developed in the AIDA and AIDA2020 projects [24]. Larger simulation and reconstruction samples were produced with the ILC DIRAC grid production tool [25, 26].

7.1.1 Event Generation

The detector performance is studied with single particles or simple event topologies. The individual particles are used to probe the track reconstruction and the particle ID. The reconstruction of particles inside jets is tested through the creation of Z-like bosons of different masses which decay into pairs of u, d, or s quarks. These events were created with WHIZARD [27, 28]. To study the track reconstruction and particle ID in complex events, and for the flavour tagging studies, $u\bar{u}$, $d\bar{d}$, $s\bar{s}$, $c\bar{c}$, $b\bar{b}$, and $t\bar{t}$ events created with WHIZARD are used. In all cases, parton showering, hadronisation, and fragmentation is performed in PYTHIA with the fragmentation parameters tuned to the OPAL data taken at LEP [3, Appendix B]. The generation of the beam-related background events (dominated by incoherent pairs and synchrotron radiation photons) are described elsewhere [4].

7.1.2 Detector Simulation

The CLD detector geometry is described with the DD4HEP software framework, and simulated in GEANT4 [29–31] via the DDG4 [32] package of DD4HEP. The GEANT4 simulations are performed with the FTFP_BERT physics list of GEANT4 version 10.02p02.

7.1.3 Event Reconstruction

The reconstruction software is implemented in the linear collider MARLIN-framework [33], the reconstruction algorithms take advantage of the geometry information provided via the DDREC [34] data structures and surfaces. If the effect of beam-induced background is to be studied, the reconstruction starts with the overlay of background events via the *overlay* processor [35], which also selects only the energy deposits inside appropriate timing windows around the physics event. In the next step, the hit positions in the tracking detectors are smeared with Gaussian distributions according to the single point resolutions per layer. The calorimeter hits are scaled with the calibration constants obtained from the reconstruction of mono-energetic 50 GeV photons and K_L^0 .

Tracking The tracking algorithm used in reconstruction at CLD is referred to as *ConformalTracking*. In modern pattern recognition algorithms, the use of cellular networks has been shown to be a powerful tool, providing robustness against missing hits and the addition of noise to the system [36]. For a detector with solenoid field and barrel plus endcap configuration, cellular automata (CA) may be applied to provide efficient track finding. Several aspects of CA algorithms may however impact performance negatively: producing many possible hit combinations requires a fit to be performed on a large number of track candidates. This may be costly in processing time. Methods to reduce combinatorics at this stage may, in turn, compromise on the final track finding performance. One way around such issues is the additional application of conformal mapping.

Conformal mapping is a geometry transform which has the effect of mapping circles passing through the origin of a set of axes (in this case the global xy plane) onto straight lines in a new uv co-ordinate system. By performing such a transform on an xy projection of the detector (where the xy plane is the bending plane of the solenoid), the pattern recognition can be reduced to a straight line search in two

386 dimensions. Cellular automata can then be applied in this 2D space, with the use of a simple linear fit to
 387 differentiate between track candidates. Figure 24 shows an example of cellular automaton in conformal
 388 space.

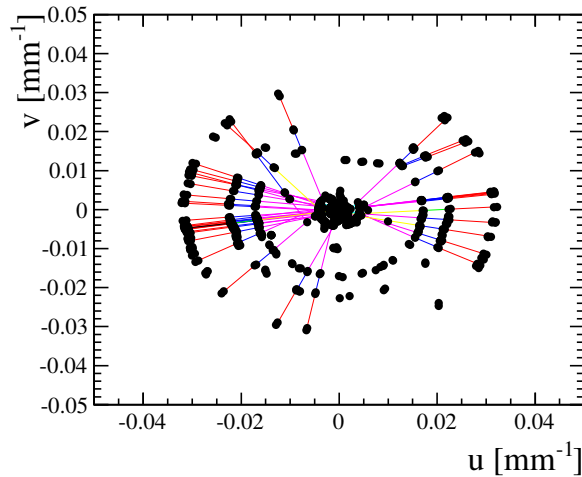


Figure 24: Cellular automaton in conformal space.

389 In order to make this approach flexible to changes in the geometry (or for application to other detector
 390 systems), all hits in conformal space are treated identically, regardless of sub-detector and layer. Cells
 391 between hits are produced within a given spatial search window, employing kd-trees for fast neighbour
 392 lookup [36]. This provides additional robustness against missing hits in any given detection layer. A
 393 second 2D linear fit in the sz parametrisation of the helix is also implemented, to recover the lost inform-
 394 ation resulting from the 2D projection onto the xy plane and reduce the number of “ghost” tracks. A
 395 minimum number of 4 hits is required to reconstruct a track.

396 For displaced tracks, which do not comply with the requirement of passing through the origin of the
 397 global xy plane, second-order corrections are applied to the transformation equations. Additionally, a
 398 strategy change has been proven necessary, in terms of:

- 399 • broader angles in the search for nearest neighbours
- 400 • minimum number of 5 hits to reconstruct a displaced track
- 401 • inverted order, from tracker to vertex hits

402 The tracks found by the pattern recognition in conformal space are then fitted in global space with a
 403 Kalman filter method. The performance studies presented in this note assume a homogeneous magnetic
 404 field of 2 T.

405 **Particle Flow Clustering** The calorimeter clusters are reconstructed in the particle flow approach by
 406 PANDORAPFA [10, 12, 37]. PANDORAPFA uses the reconstructed tracks and calorimeter hits as input
 407 to reconstruct all visible particles. The procedure is optimised to achieve the best jet energy resolution.
 408 This may not be the ideal procedure for isolated particles, which can benefit from a dedicated treatment.
 409 The output of the particle flow reconstruction are *particle flow objects* (PFOs).

410 7.1.4 Treatment of Background

411 The largest impact on the detector performance from beam-induced backgrounds comes in the form of
 412 incoherent e^+e^- pairs and photons from synchrotron radiation. When studying the detector performance

413 degradation due to these backgrounds, the following number of bunch crossings (with 1 background
414 event per bunch crossing) are overlaid to the physics event, placed at bunch crossing 1:

- 415 • at 91.2 GeV centre-of-mass energy: 20 bunch crossings
- 416 • at 365 GeV centre-of-mass energy: 3 bunch crossings

417 All hits inside the time window are then passed forward to the reconstruction.

418 Given the different bunch spacing at the two energies (19.6 ns at 91.2 GeV, 3396 ns at 365 GeV), the
419 number of overlaid bunch crossings corresponds to a detector integration time of, respectively, 400 ns and
420 10 μ s. The latter is in accordance with the assumed vertex and tracker readout time (see section 3.3). The
421 overlay of 20 background events (400 ns integration time at 91.2 GeV), on the other hand, is currently
422 imposed by a limitation from software/computing.

423 Once the particle flow clustering is finished, additional p_T dependent timing cuts may be applied.
424 Depending on the particle type—photon, neutral hadron, or charged particle—and the transverse mo-
425 mentum and based on the time of the clusters, reconstructed particles may be rejected. The time of a
426 cluster is the truncated energy weighted mean time of its hits. For CLICdet, a set of timing cuts was
427 defined to reduce the impact of $\gamma\gamma \rightarrow$ hadrons background events, as described in Appendix B of the
428 CDR [3]. In the case of CLD, future studies of jet performances including beam induced background
429 events will have to determine whether a similar strategy is needed (the rate of $\gamma\gamma \rightarrow$ hadrons events at
430 CLD is less than 0.01 events per bunch crossing, and should be negligible).

431 7.2 Performance of Lower Level Physics Observables

432 7.2.1 Single Particle Performances

433 **Position, Angular and Momentum Resolutions** The results in this section demonstrate the combined
434 performance of the tracking system (vertex and tracker subdetectors) with those of the tracking algorithm,
435 described in Sec. 7.1.3.

To identify heavy-flavour quark states and tau-leptons with high efficiency, a precise measurement of
the impact parameter and of the charge of the tracks originating from the secondary vertex is required.
Monte Carlo simulations for linear collider experiments [3] show that these goals can be met with a
constant term in the transverse impact-parameter resolution of $a \simeq 5 \mu\text{m}$ and a multiple-scattering term
of $b \simeq 15 \mu\text{m}$, using the canonical parameterisation

$$\sigma(d_0) = \sqrt{a^2 + b^2 \cdot \text{GeV}^2 / (p^2 \sin^3(\theta))}. \quad (2)$$

436 Figure 25 shows the impact-parameter resolutions obtained for CLD, for isolated muon tracks with
437 momenta of 1, 10 and 100 GeV. Each data point corresponds to 10 000 muons at fixed energy and po-
438 lar angle. For each dataset, the resolution is calculated as the width of the Gaussian fit of the residual
439 distributions, i.e. the difference between the reconstructed and simulated parameters per track. In Fig-
440 ure 25(a), superimposed to the data points for the transverse impact parameter resolution are the curves
441 obtained with Eq. 2 for the different energies. High-energy muons show a resolution well below the
442 high-momentum limit of $5 \mu\text{m}$ at all polar angles, while for 10 GeV muons this is achieved only for
443 central tracks above 30° . The data points for 1 GeV muons are systematically above the parametrization,
444 but only by 10-15%. The achieved longitudinal impact-parameter resolution, shown in Figure 25(b), for
445 muons at all energies and polar angles is smaller than the longitudinal bunch length of 1.5 mm at the
446 highest collision energy.

447 The dependence of the impact-parameter resolution on the pixel technology has been studied by vary-
448 ing the single point resolution for the vertex layers from the baseline value of $3 \mu\text{m}$ to $5 \mu\text{m}$ and $7 \mu\text{m}$.

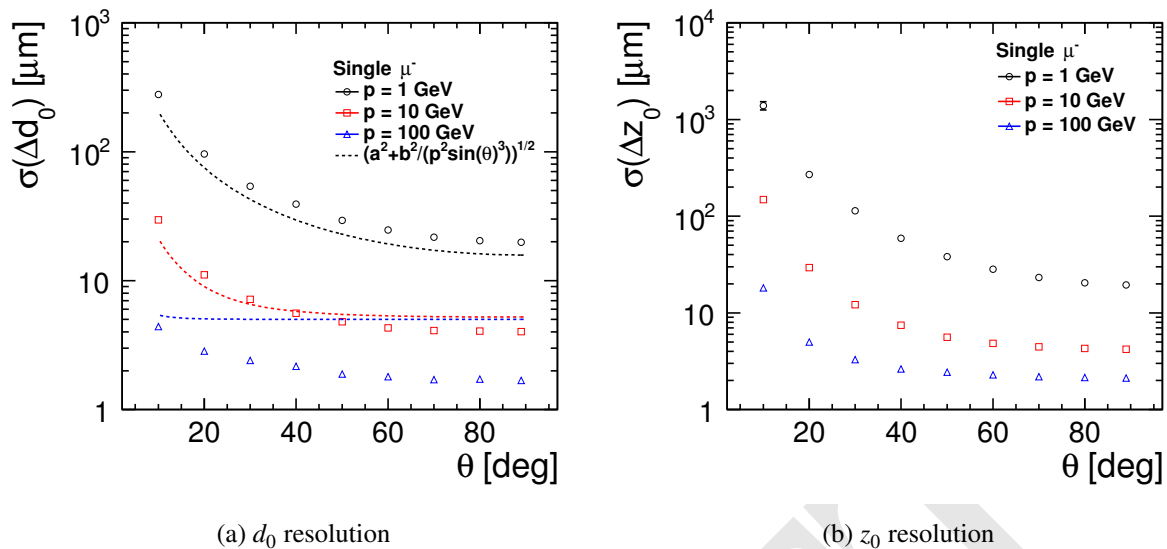


Figure 25: Impact-parameter resolutions, obtained with the baseline vertex detector layout for CLD, in the transverse (a) and in the longitudinal (b) plane, for muon tracks with momenta of 1, 10 and 100 GeV. Also shown is the parametrisation of Equation 2 with the target values $a = 5 \mu\text{m}$ and $b = 15 \mu\text{m}$.

449 The resulting resolutions are shown in Figure 26. The single point resolution dominates at higher ener-
 450 gies, especially in the barrel region, where a change from 3 to 5 μm results in an increase by approx-
 451 imately 80% and 50% for d_0 and z_0 resolutions respectively. However, even in the worst scenario of
 452 7 μm single point resolution, the d_0 resolution for 100 GeV tracks does not exceed the target value for
 453 the high-momentum limit of $a \simeq 5 \mu\text{m}$. For the 10 GeV tracks, on the other hand, the resolution is at the
 454 limit. For 1 GeV muons, for which multiple scattering dominates, the effect of a single point resolution
 455 variation from 3 to 5 μm amounts to maximum 6%.

456 The detector performance depends on the spatial resolution in the silicon detectors, which is defined
 457 by the pixel and strip sizes. The default single point resolutions in the simulation model are:

- 458 • vertex barrel and discs: 3 μm x 3 μm
- 459 • inner tracker barrel and discs: 7 μm x 90 μm
- 460 – except first inner tracker discs: 5 μm x 5 μm
- 461 • outer tracker barrel and discs: 7 μm x 90 μm

462 So far no detailed cooling studies have been performed. Adopting the ALICE ITS upgrade concept, as
 463 described in Sec. 3.3, has been a first attempt in including material to account for water cooling. In order
 464 to test the sensitivity of the performance to assumptions about cooling, supports and cabling, the material
 465 budget of the CLD vertex detector has been further increased by 50%. Results for the impact-parameter
 466 resolution with this additional material are shown in Figure 27, together with the CLD baseline. As
 467 expected, low-momentum tracks are the most affected by the change in the material budget, while the
 468 effect is negligible for tracks of 100 GeV. However, it is encouraging to notice that the biggest variation,
 469 on 1 GeV tracks, amounts to only 10%.

470 Figure 28 shows the polar angular resolution (left) and the azimuthal angular resolution (right), both
 471 as a function of the polar angle θ , for muon tracks of 1, 10 and 100 GeV. Both resolutions improve while
 472 moving from the forward to the transition region and then level up in the barrel. The only exception is
 473 the trend of the θ resolution for high energy muons, as it increases in the barrel region, where the single

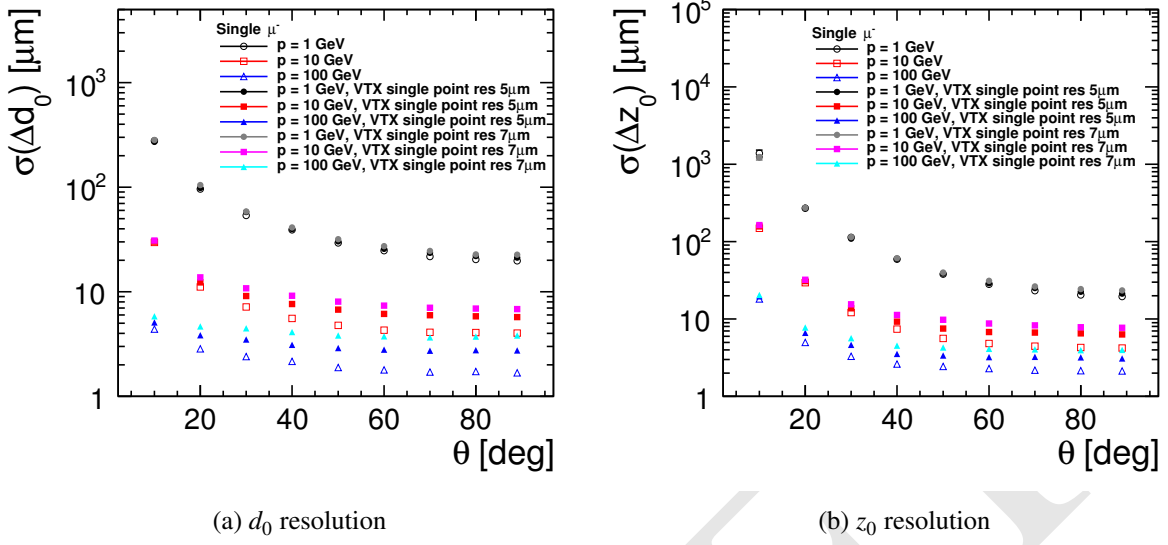


Figure 26: Impact-parameter resolution as a function of polar angle in the transverse (a) and in the longitudinal (b) plane, for muon tracks with momenta of 1, 10 and 100 GeV. Empty markers refer to the baseline vertex detector with single point resolution of $3 \mu\text{m}$. Two other sets of curves are plotted, which correspond to a single point resolution in the vertex detector of $5 \mu\text{m}$ and $7 \mu\text{m}$ respectively.

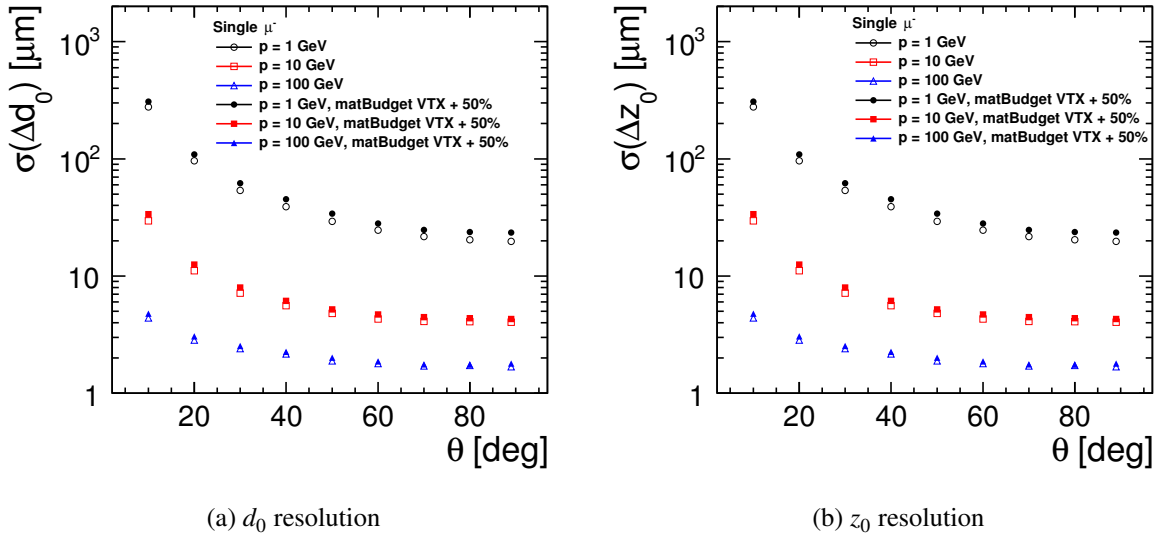


Figure 27: Impact parameter resolution as a function of polar angle in the transverse (a) and in the longitudinal (b) plane, for muon tracks with momenta of 1, 10 and 100 GeV. Empty markers refer to the baseline CLD vertex detector. Results shown with full markers are obtained with a detector model with the material budget in the vertex increased by 50% with respect to CLD.

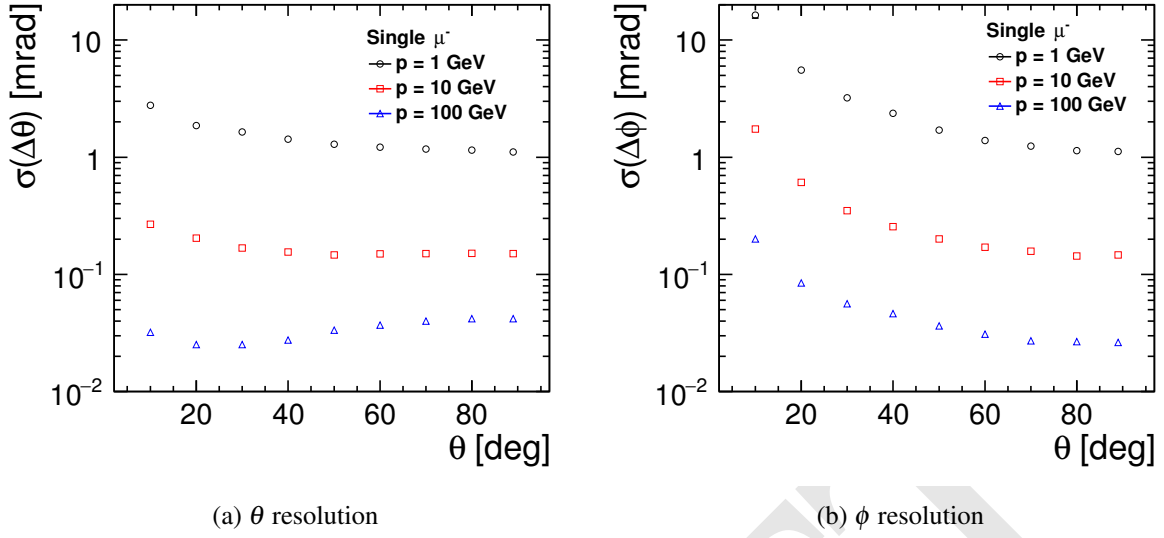


Figure 28: Polar (a) and azimuthal (b) angular resolution as a function of polar angle for muon tracks with momenta of 1, 10 and 100 GeV.

474 point resolution becomes dominant. For the high energy muons, the ϕ resolution reaches a minimum of
 475 0.025 mrad in the barrel and the θ resolution reaches the same value in the transition region.

The p_T resolution $\sigma(\Delta p_T/p_T^2)$ for single muons is determined from a single Gaussian fit of the distribution $(p_{T,MC} - p_{T,rec})/p_{T,MC}^2$ and is shown in Figure 29 as a function of the momentum p and of the polar angle θ . Dashed lines correspond to the fit of the data points according to the parametrisation:

$$\sigma(\Delta p_T/p_T^2) = a \oplus \frac{b}{p \sin^{3/2} \theta} \quad (3)$$

476 where parameter a represents the contribution from the curvature measurement and parameter b is the
 477 multiple-scattering contribution. The values of these parameters for the different curves are summarized
 478 in Table 14. A p_T resolution of $5 \cdot 10^{-5} \text{ GeV}^{-1}$ is achieved for 100 GeV tracks in the barrel. The cross-
 479 over observed between the high-energy muons at 70° and 89° has been investigated and its origin has
 480 been traced back to the track fit resulting in too small uncertainties on the track parameters at 89° . These
 481 small uncertainties cause the pull distributions to be broader, thus the resolution to be worse than at 70° .
 482 Improvements in the track fitting are being developed, and are expected to restore the resolution for
 483 89° tracks to a similar value as for 70° tracks. For low-momentum tracks, mainly in the very forward
 484 region, the data points slightly deviate from the parametrisation due to the multiple scattering becoming
 485 dominant.

Table 14: Fit parameters from Eq. 3

deg	a	b
10	$5.6 \cdot 10^{-5}$	0.010
30	$1.7 \cdot 10^{-5}$	0.005
50	$1.2 \cdot 10^{-5}$	0.004
70	$1.6 \cdot 10^{-5}$	0.003
89	$2.5 \cdot 10^{-5}$	0.003

GeV	a	b
1	$5 \cdot 10^{-3}$	0.008
10	$4 \cdot 10^{-4}$	0.007
100	$2 \cdot 10^{-5}$	0.006

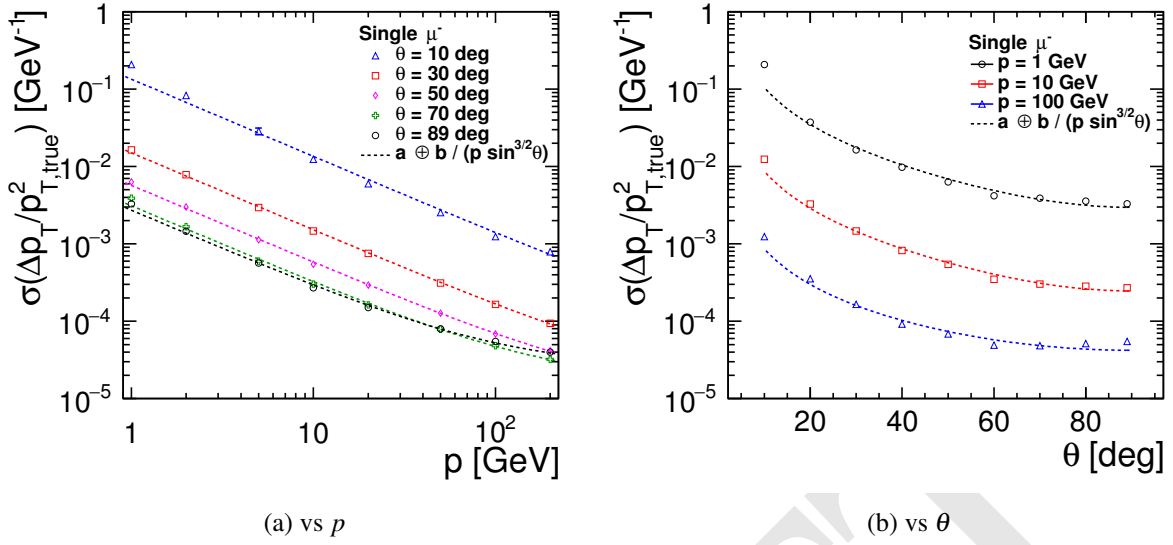


Figure 29: Transverse momentum resolution for single muons as a function of momentum at fixed $\theta = 10^\circ, 30^\circ, 50^\circ, 70^\circ$ and 89° (a) and as a function of polar angle at fixed momentum $p = 1, 10$ and 100 GeV (b). The dashed lines show a fit to the parametrisation given in Equation 3. The fitted parameters are given in Table 14.

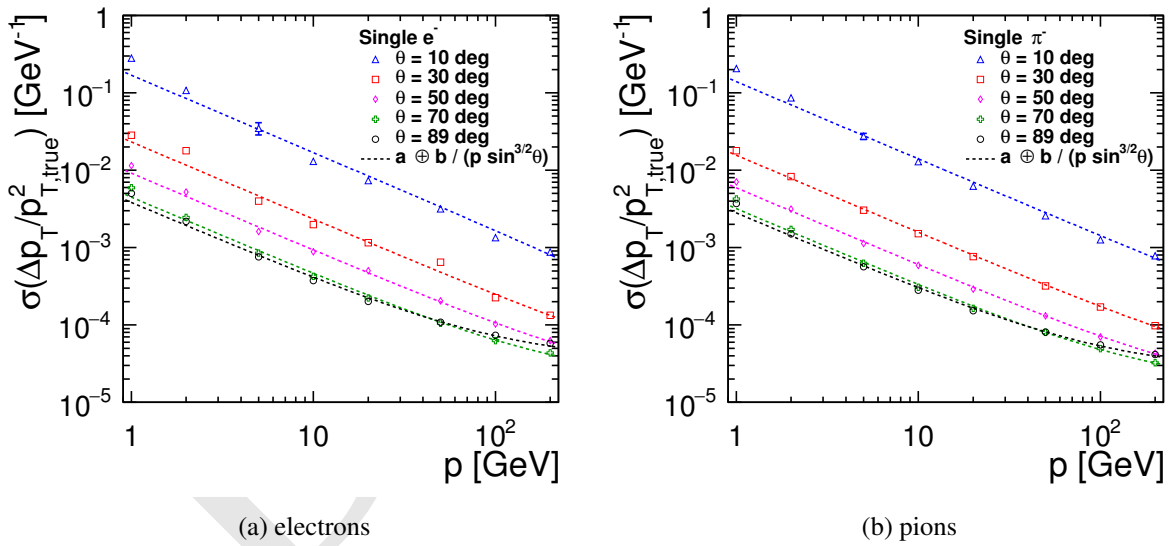


Figure 30: Transverse momentum resolution as a function of momentum at fixed $\theta = 10^\circ, 30^\circ, 50^\circ, 70^\circ$ and 89° for single electrons (left) and for single pions (right). The dashed lines show a fit to the parametrisation given in Equation 3.

486 Similarly, the momentum resolution for isolated electron and pion tracks was studied and is shown in
 487 Figure 30, to test the tracking performance for other particles than muons. The resulting performances
 488 at high energies are very similar to those for isolated muon tracks.

489 **Tracking Efficiency** Tracking efficiency is defined as the fraction of the reconstructable Monte Carlo
 490 particles that have been reconstructed. A particle is considered reconstructable if it is stable at generator
 491 level (`getStatus = 1`), if $p_T > 100$ MeV, $|\cos(\theta)| < 0.99$ and if it has at least 4 unique hits (i.e. hits which
 492 do not occur on the same subdetector layer).

493 The efficiency for isolated muon tracks, shown in Figure 31 has been computed by reconstructing 2
 494 million muons simulated at polar angles $\theta = 10^\circ, 30^\circ, 89^\circ$ and with a power-law energy distribution
 495 (maximum energy 250 GeV) in order to favour statistics at low- p_T . The tracking efficiency is around
 496 100% for single tracks with transverse momentum greater than 500 MeV, except in the very forward
 497 region (10°) for which a loss of 0.5% is observed. This small inefficiency stems from an artefact of the
 498 tracking algorithm: When the muon has released a low-energy electron (delta ray), there can be confusion
 499 in picking the hits from the primary muon or the secondary electron. This is mainly an issue for very
 500 forward tracks, since they traverse more material in the vertex detector and the probability of delta ray
 501 production is enhanced. Further improvements to the tracking software should be able to remedy this
 502 issue.

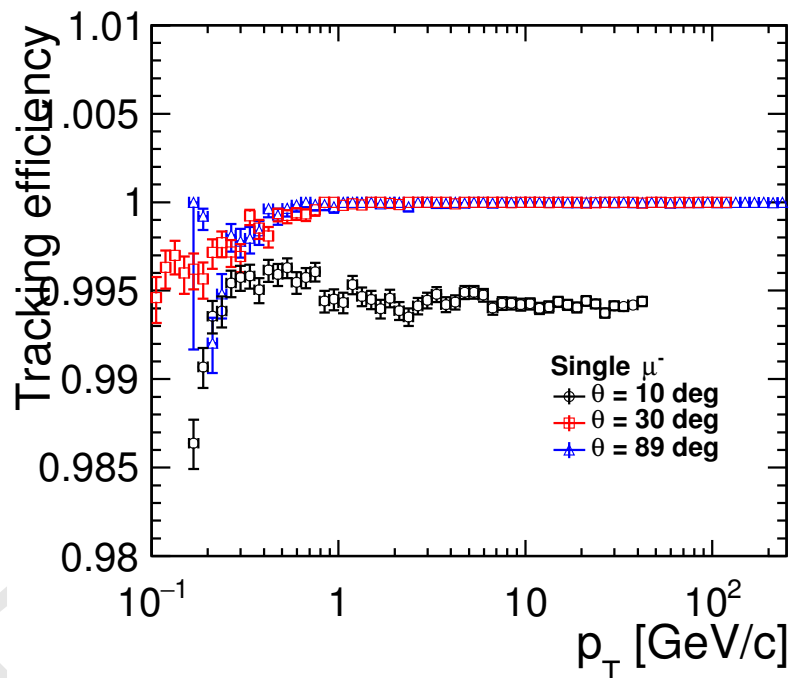


Figure 31: Tracking efficiency as a function of p_T for muons with energies up to 250 GeV, at polar angles $\theta = 10^\circ, 30^\circ, 89^\circ$. The efficiency at the lowest p_T for $\theta = 10^\circ$ is off scale (around 0.96). The efficiency at the lowest p_T for $\theta = 89^\circ$ is not shown since these particles do not have the required number of hits.

503 Figure 32 shows the same efficiency as a function of polar angle (left) and azimuthal angle (right). The
 504 drop in the forward region (below 20°) is consistent with what is shown in Figure 31. The oscillation
 505 pattern shown in Fig. 32(b) reflects the position of overlaps between modules of the layers.

506 Similarly, the tracking efficiency for 2 million isolated electrons and pions simulated at polar angles
 507 $\theta = 10^\circ, 30^\circ$ and 89° and with a power-law energy distribution, is shown in Figure 33. For electrons at
 508 30° and 89° , the efficiency reaches 100% above 1 GeV. For electrons at 10° , a similar trend as for muons
 509 is observed, with a loss of the same order of 0.5%. At low transverse momentum, at any of the probed
 510 angles, the efficiency does not drop below to a minimum of 98%. The trend for pions at 10° does not
 511 differ from that of electrons at the same angle. The efficiency for pions at 30° and 89° is 100% down to

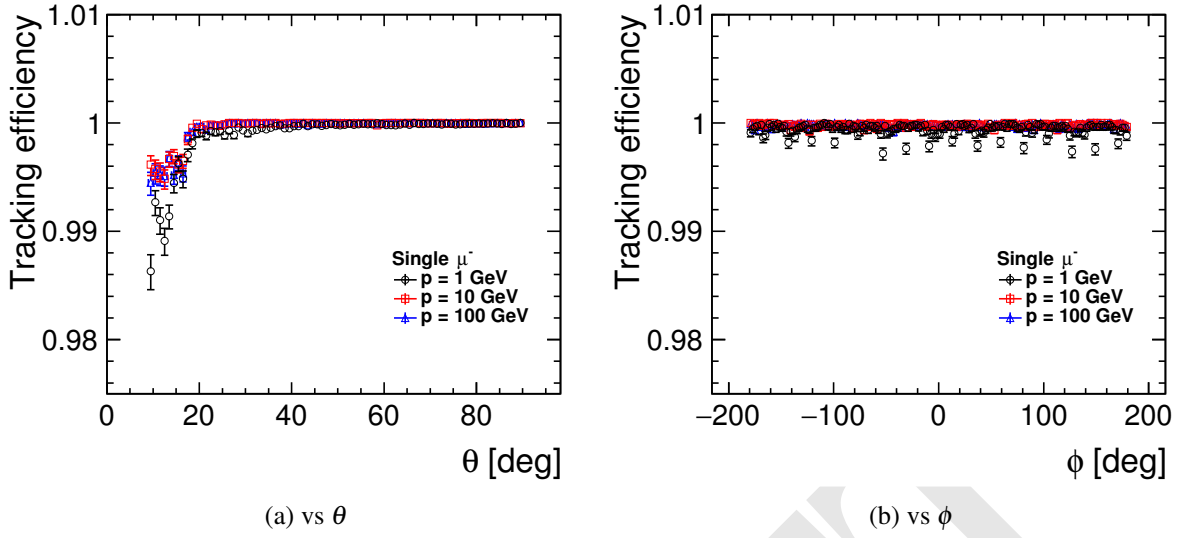


Figure 32: Tracking efficiency as a function of polar (a) and azimuthal (b) angle for muons with momenta of 1, 10 and 100 GeV.

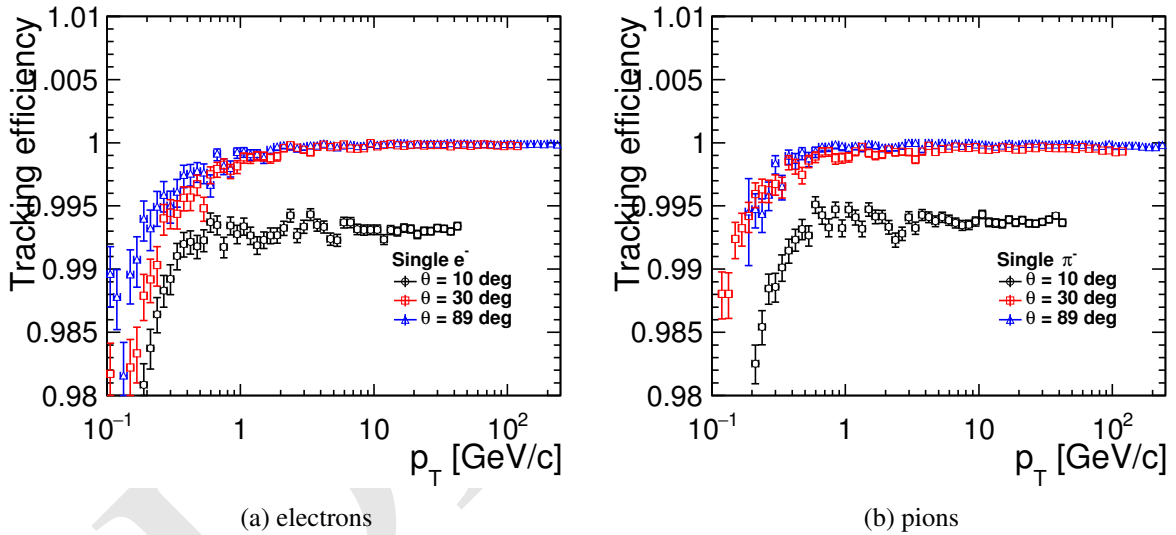


Figure 33: Tracking efficiency vs p_T for electrons (left) and pions (right).

512 600 MeV, and it drops slightly, but remains above 99%, for lower- p_T tracks.

513 To probe the tracking performance for displaced tracks, 10000 single muons have been simulated,
 514 requiring their production vertex to be within $0 \text{ cm} < y < 60 \text{ cm}$ and their angular distribution in a cone
 515 of 10° width around the y axis, i.e. $80^\circ < \theta, \phi < 100^\circ$. This is done so that particles are produced
 516 in the barrel region only and they traverse roughly the same amount of material. The efficiency as a
 517 function of production vertex radius, i.e. $\sqrt{x^2 + y^2}$, is shown in Figure 34 for muons with momenta of
 518 1, 10 and 100 GeV. For 1 GeV muons the efficiency is around 100%, except for those that are produced
 519 after the first two vertex barrels (radius $R > 38 \text{ mm}$), for which the efficiency drops by 20%, due to
 520 the fact that due to losing energy while traversing the detector layers, some particles have not enough
 521 left-over momentum to leave the required minimum number of hits. For higher-energy muons, instead,
 522 the efficiency is constantly 100%. Regardless of the energy, an abrupt fall-off is observed for all tracks

523 with a production radius of 400 mm or more. This is an effect of the reconstruction cuts, since for
524 displaced tracks a minimum number of 5 hits is required to make the track, while only 4 sensitive layers
525 are traversed by tracks starting beyond $R = 400$ mm.

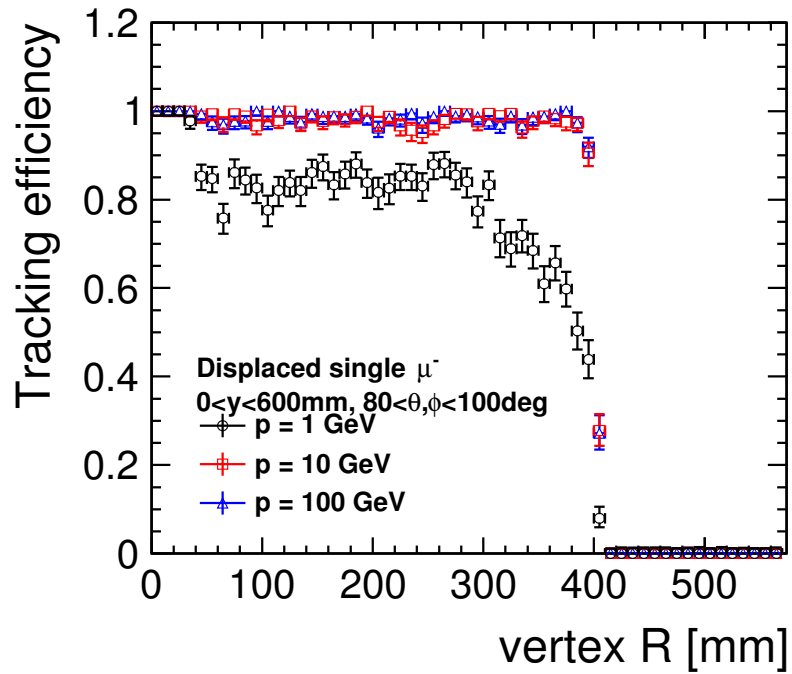


Figure 34: Tracking efficiency as a function of production vertex radius for muons with momenta of 1, 10 and 100 GeV, uniformly generated in a range $0 < y < 600$ mm and $80^\circ < \theta, \phi < 100^\circ$.

526 **Particle Reconstruction and Identification** Particles are reconstructed and identified using the PAN-
 527 DORAPFA C++ Software Development Kit [12]. The particle flow reconstruction algorithms of Pan-
 528 dora have been studied extensively in full GEANT4 simulations of the ILD and the CLIC_ILD detector
 529 concept [37] as well as of CLICdet. Particle flow aims to reconstruct each visible particle in the event
 530 using information from all subdetectors. The high granularity of calorimeters is essential in achieving the
 531 desired precision measurements. Electrons are identified using clusters largely contained within ECAL
 532 and matched with a track. Muons are determined from a track and a matched cluster compatible with a
 533 minimum ionizing particle signature in ECAL and HCAL, plus corresponding hits in the muon system.
 534 A hadronic cluster in ECAL and HCAL matched to a track is used in reconstructing charged hadrons.
 535 Hadronic clusters without a corresponding track give rise to neutrons, and photons are reconstructed from
 536 an electromagnetic cluster in ECAL. In jets typically 60% of the energy originates from charged hadrons
 537 and 30% from photons. The remaining 10% of the jet energy are mainly carried by neutral hadrons.

538 The performance of the Pandora reconstruction algorithms is studied in single particle events at several
 539 energies, generated as flat distributions in $\cos\theta$. The ECAL energy resolution is studied using single
 540 photon events. At each energy point in three different regions (barrel, endcap, and transition region) the
 541 photon energy response distribution is iteratively fitted with a Gaussian within a range $\pm 3\sigma$. The σ of
 542 the Gaussian is a measure for the energy resolution in ECAL. The energy dependence of the photon
 543 energy resolution of CLD is shown in Figure 35(a), for the three detector regions. The stochastic term is
 544 $15\%/\sqrt{E}$, determined from a two parameter fit within the energy range of 5 and 100 GeV.

545 For hadrons the HCAL hits are reweighted using the software compensation technique implemented
 546 within Pandora, and developed by the CALICE (Calorimeter for Linear Collider Experiment) collabora-
 547 tion [38, 39]. In the non-compensating calorimeters of CLD the detector response for electromagnetic
 548 subshowers is typically larger than for hadronic showers. On average the electromagnetic component
 549 of the shower has larger hit energy densities. The weights depend on the hit energy density and the
 550 unweighted energy of the calorimeter cluster, where hits with larger hit energy densities receive smaller
 551 weights. In a dedicated calibration procedure within Pandora, software compensation weights are deter-
 552 mined using single neutron and K_L^0 events over a wide range of energy points. At each energy point

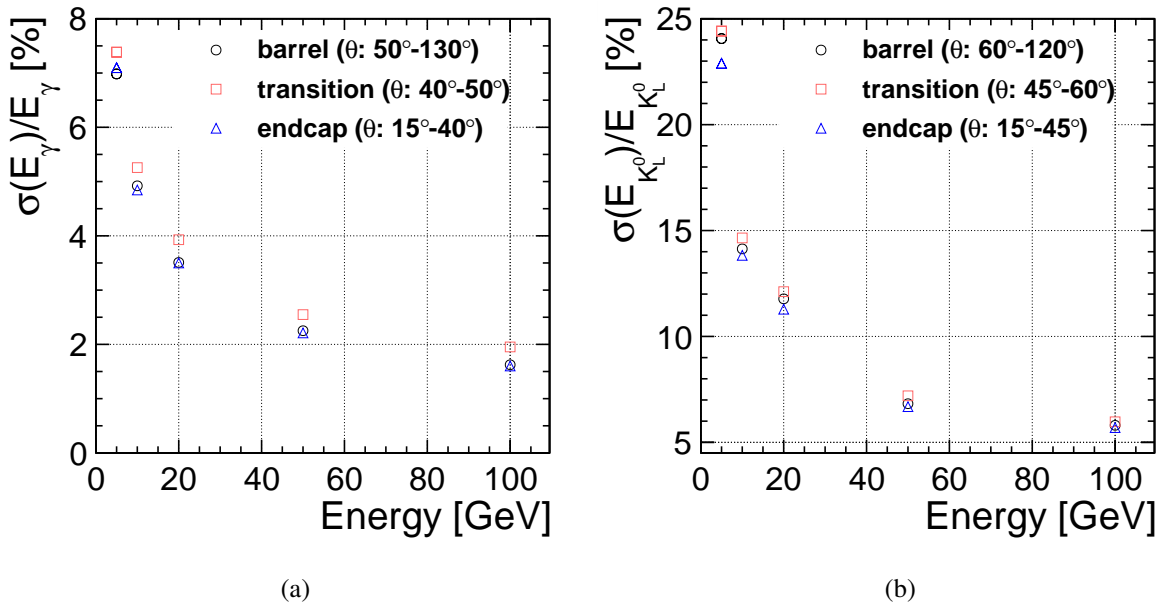


Figure 35: Photon energy resolution (a) and neutral hadron resolutions of K_L^0 's (b) as a function of energy. Results are shown for the barrel region, transition region and endcap.

553 equal statistics is required, i.e. using the same number of events for neutrons and K_L^0 . Only events with
 554 one cluster fully contained within ECAL plus HCAL are used in this calibration. Software compensation
 555 improves the energy resolution of hadronic clusters. The resulting energy resolution of neutral hadrons
 556 is shown for K_L^0 as a function of energy in Figure 35(b).

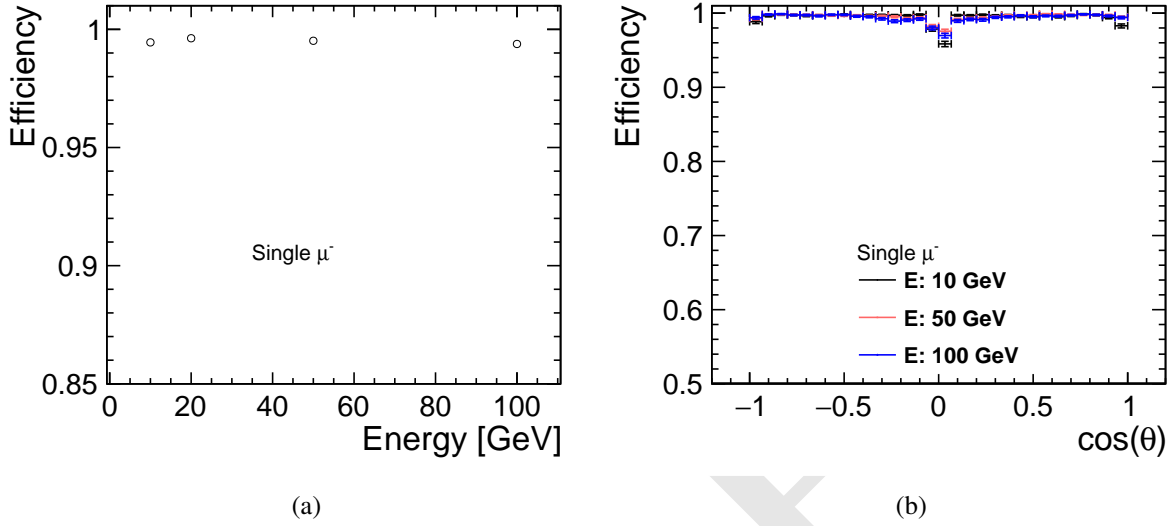


Figure 36: Particle identification efficiency for muons as function of energy (a) and as function of $\cos \theta$ for three different energies (b).

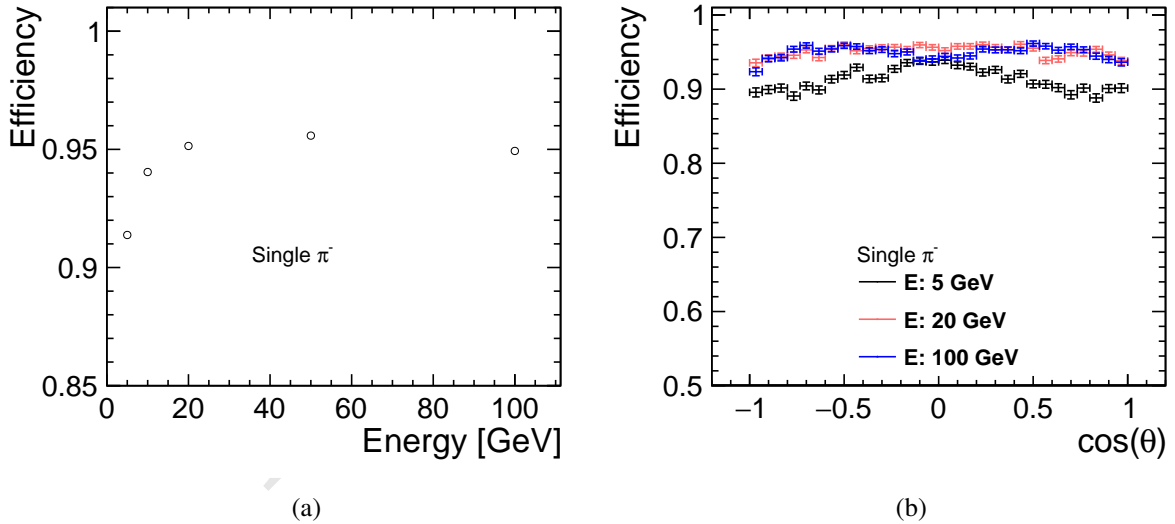


Figure 37: Particle identification efficiency for pions as function of energy (a) and as function of $\cos \theta$ for three different energies (b).

557 The particle identification efficiency of Pandora particle flow algorithms is studied in single particle
 558 events separately for muons, electrons, photons and pions. The events are produced as flat distributions
 559 in $\cos \theta$. The reconstructed particle is required to be of the same type as the “true” particle. It has
 560 to satisfy angular matching criteria $|\phi_{reconstructed} - \phi_{true}| < 2$ mrad and $|\theta_{reconstructed} - \theta_{true}| < 1$ mrad.
 561 The reconstructed transverse momentum of charged particles has to be within 5% of the transverse mo-
 562 mentum of the “true” particle. The particle identification efficiency is studied as function of energy and

563 $\cos \theta$. The result for muons is illustrated in Figure 36(a) as function of energy and in Figure 36(b) as
 564 function of the $\cos \theta$. The efficiency is beyond 99% for all energies, flat as function of $\cos \theta$. The effi-
 565 ciency of pion identification is about 90% at low energies, 94–95% at energies from 20 GeV up to 100
 566 GeV (Figure 37(a)), and flat as function of $\cos \theta$ (Figure 37(b)).

567 While for muons and pions the energy is accurately reconstructed, for electrons the reconstructed
 568 energy has, due to Bremsstrahlung, a long tail towards lower values compared to the true energy. A
 569 simple Bremsstrahlung recovery algorithm is applied which uses close by photons (within $|\phi_{reconstructed} -$
 570 $\phi_{true}| < 20$ mrad and $|\theta_{reconstructed} - \theta_{true}| < 1$ mrad) to dress the electron momentum by summing their
 571 four momenta. Additionally, reconstructed electrons, which were dressed with photons, are required to
 572 satisfy a looser energy matching requirement (reconstructed energy by the calorimeter has to be within
 573 $5 \sigma_E$) since part of their energy has been measured by the calorimeter only.

574 The electron identification efficiency as a function of energy is shown in Figure 38(a). For energies of
 575 about 20 GeV and higher, the efficiencies reach 95%. Efficiency in the endcap and barrel are similar, as
 576 can be seen in Figure 38(b). In the transition region the efficiency is 5%–10% lower than in the barrel or
 577 endcaps individually.

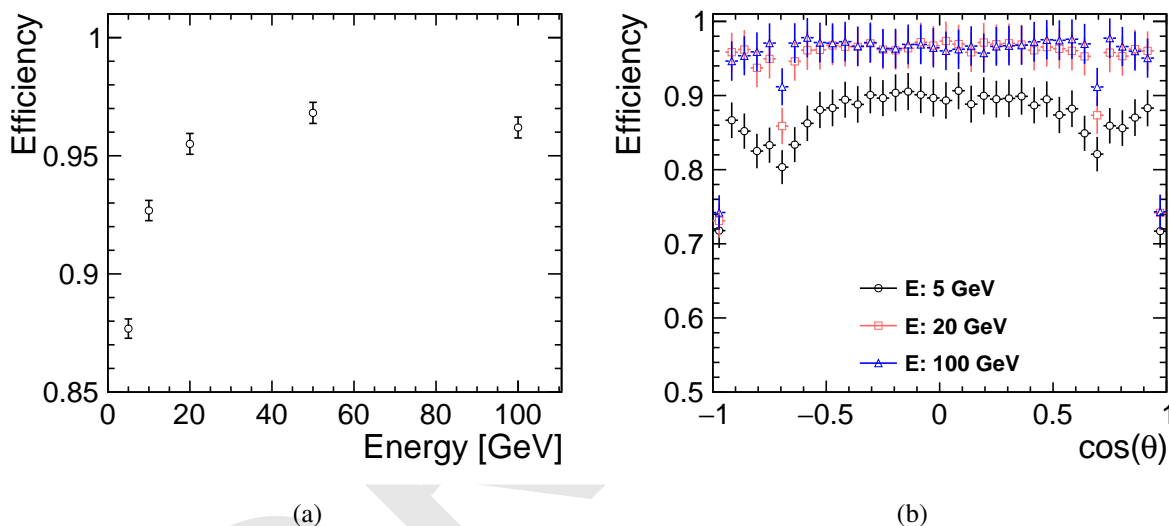


Figure 38: Particle identification efficiency for electrons as function of energy (a) and as function of $\cos \theta$ for three different energies.

578 For single photons, the signatures for unconverted and converted photons are considered separately.
 579 The fraction of converted photons is around 12% overall, for all energy points. This fraction increases
 580 from around 8% at 90° to around 20% for very forward polar angles. The particle identification efficiency
 581 for unconverted and converted photons is shown in Figure 39. Reconstructed photons are required to sat-
 582 isfy the same spatial matching criteria as charged particles and their reconstructed energy has to be within
 583 $5 \sigma_E$ (based on the two parameter fit on the resolution curves shown in Figure 35(a)). For unconverted
 584 photons the identification efficiency is beyond 99% for all energies (Figure 39(a)).

585 For converted photons, requiring only angular matching results in a high identification efficiency at
 586 high energies, reaching 83% at 50 GeV. Adding the energy matching criterion to the leading photon in
 587 the event leads to a strongly reduced efficiency, as expected (see the red squares in Figure 39(b)). In many
 588 conversion events Pandora running in its default configuration reconstructs two photons. Merging both
 589 reconstructed candidate clusters, if they are within $|\phi_{reconstructed} - \phi_{true}| < 20$ mrad and $|\theta_{reconstructed} -$
 590 $\theta_{true}| < 1$ mrad, and applying the identification criteria on the merged candidate, significantly improves
 591 the efficiency for the angular and energy matched case (see the blue triangles in Figure 39(b)).

592 Around 60% of all conversions occur before reaching the last 4 layers of the tracker. The tracking

593 algorithm requires at least four hits in the tracker. Work has started on a CLICdet/CLD specific conver-
 594 sion algorithm in Pandora which should improve identification of converted photons particularly at low
 595 energies.

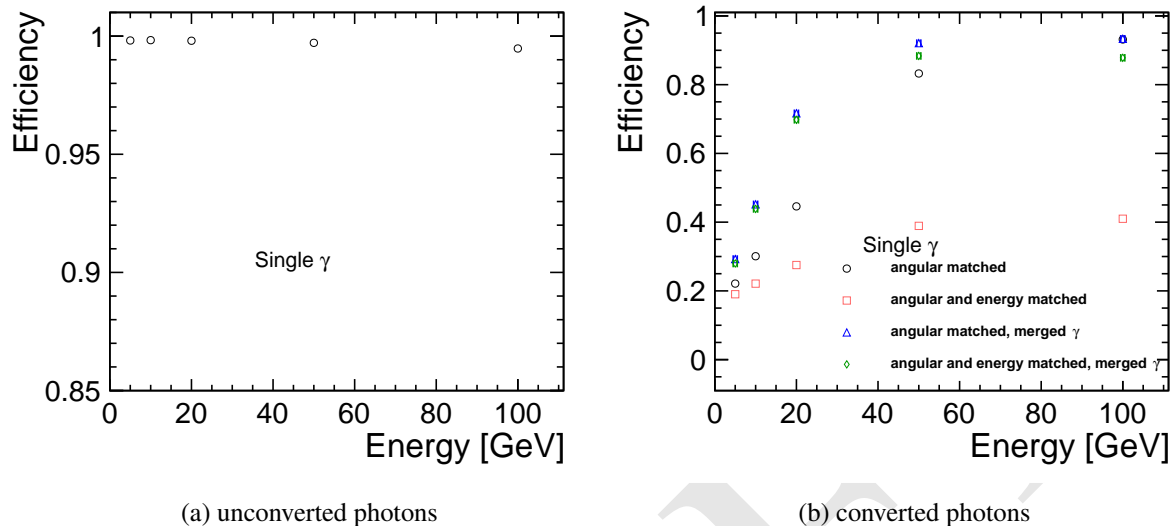


Figure 39: Particle identification efficiency for unconverted (a) and converted photons (b) as a function of energy. In the case of unconverted photons, the efficiency is shown when requiring either angular, or angular and energy, matching. In the case of converted photons both criteria are, additionally, applied after merging leading photon candidates (i.e. their electromagnetic clusters) into one new photon candidate.

596 7.2.2 Performances for Complex Events

597 **Tracking Efficiency** The tracking efficiency for particles in jets has been studied in samples at the
 598 lowest (91.2 GeV) and highest (365 GeV) centre-of-mass energy at which the FCC-ee is designed to
 599 operate. The tracking performances for the same physics samples have been analyzed also with the
 600 overlay of incoherent e^+e^- pairs. A study of the effect from overlaying synchrotron radiation background
 601 events is in preparation.

602 In the following, results will be presented for 10 000 events of Z-like bosons of 365 GeV mass decaying
 603 into two light quark jets, with and without background overlay. A comparison with events of Z-like
 604 bosons of 91.2 GeV mass is also shown. Finally, tracking efficiency and fake rate are studied for tracks
 605 in $b\bar{b}$ events at 365 GeV.

606 Efficiency is defined as the fraction of reconstructable Monte Carlo particles which have been re-
 607 constructed as *pure* tracks. A track is considered pure if most of its hits ($\geq 75\%$) belong to the same
 608 Monte Carlo particle. The definition of a reconstructable particle is the same as given for single particle
 609 efficiency.

610 In jet events, the vicinity of other particles may affect the performance of the pattern recognition in
 611 assigning the right hits to the proper track. Therefore, the tracking efficiency in events of Z-like bosons
 612 of 365 GeV mass decaying to light quarks has been monitored as a function of the distance of the closest
 613 Monte Carlo particle. The latter is defined as $\sqrt{(\Delta\eta)^2 + (\Delta\phi)^2}$, where η is the pseudorapidity. The
 614 efficiency is shown in Figure 40, in which the following cuts are applied: $10^\circ < \theta < 170^\circ$, $p_T > 1$ GeV
 615 and production radius smaller than 50 cm. Results with and without overlay are comparable within
 616 statistical errors. A standard cut of 0.02 rad on the distance of closest Monte Carlo particle has been
 617 agreed on and is applied in all following tracking efficiency results.

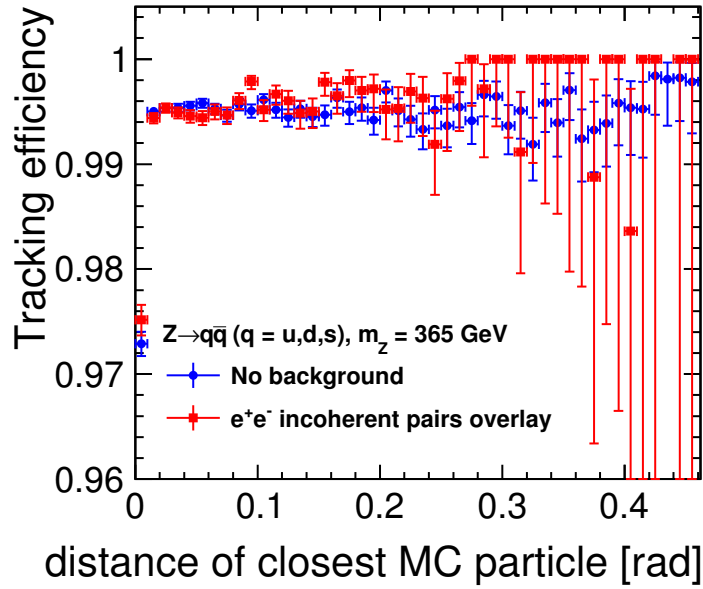


Figure 40: Tracking efficiency as a function of distance of closest MC particle for Z-like boson events decaying into light quarks, with $m_Z = 365$ GeV, with and without background overlay.

618 Figure 41 shows the tracking efficiency in events of Z bosons of 365 GeV as a function of transverse
 619 momentum, with and without overlay. The following cuts are applied for each particle in this plot:
 620 $10^\circ < \theta < 170^\circ$, distance of closest Monte Carlo particle larger than 0.02 rad and production radius
 621 smaller than 50 mm. Above 500 MeV, the tracking efficiency is constant at around 99%, while below
 622 500 MeV it goes down to a minimum of 90%. The effect of background, slightly visible in the low- p_T
 623 region, is otherwise negligible.

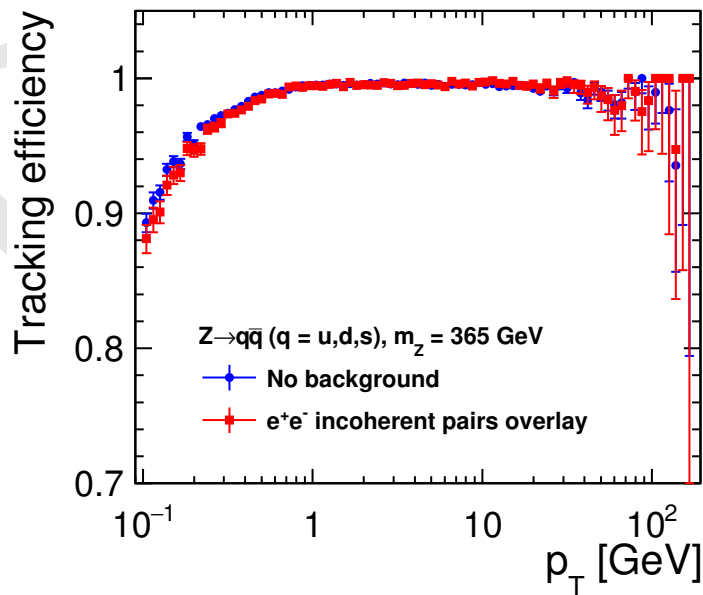


Figure 41: Tracking efficiency as a function of p_T for Z-like boson events decaying into light quarks, with $m_Z = 365$ GeV, with and without background overlay.

624 For the same events, the tracking efficiency is shown in Figure 42 as a function of polar (left) and
 625 azimuthal angle (right). The following cuts are applied in this plot: $p_T > 1$ GeV, distance of closest
 626 Monte Carlo particle larger than 0.02 rad and production radius smaller than 50 mm. The tracking
 627 efficiency approaches 100% for very central tracks and is around 99% moving towards the forward
 628 region. The minimum is reached for very forward tracks, i.e. at 10° , consisting in a maximum efficiency
 629 loss of 5% within statistical uncertainties. The dependence on the azimuthal angle is flat and does not
 630 show any particular issue. In both figures, the impact of incoherent pairs is observed to be small.

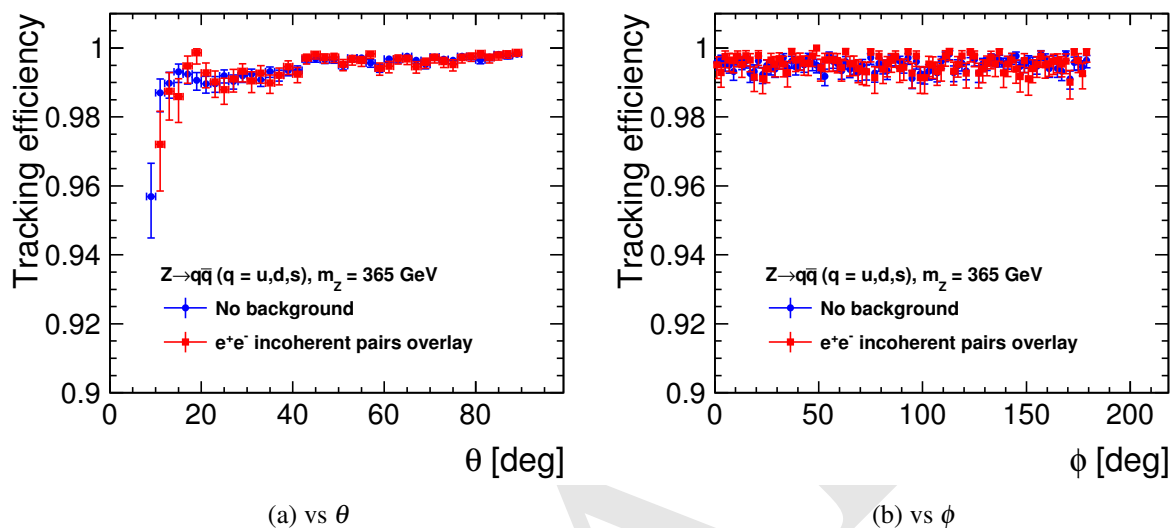


Figure 42: Tracking efficiency as a function of polar (a) and azimuthal (b) angle for Z-like boson events decaying into light quarks, with $m_Z = 365$ GeV, with and without background overlay.

631 Finally, the tracking efficiency as a function of the production vertex radius is shown in Figure 43.
 632 In this plot, the following cuts are applied: $p_T > 1$ GeV, $10^\circ < \theta < 170^\circ$ and distance of closest MC
 633 particle > 0.02 rad. The trend reflects the same behaviour observed for single displaced low-momentum
 634 muons in Figure 34, since the low-energy component of the particle spectrum dominates. The effect of
 635 background from incoherent pairs is negligible.

636 Figure 44 shows the analogous as Figure 41 for events with Z-like bosons of 91.2 GeV mass, with and
 637 without background overlay. The tracking performs equally well at both centre-of-mass energies.

638 The tracking performance has been completed by studying $b\bar{b}$ events at 365 GeV, in terms of efficiency
 639 and fake rate, the latter being the fraction of *impure* tracks out of the total reconstructed tracks. A track
 640 is considered impure if less than 75% of its hits belong to the same Monte Carlo particle.

641 Figure 45 shows efficiency (left) and fake rate (right) as a function of transverse momentum. In
 642 Figure 45(a), the following cuts are applied for each particle: $10^\circ < \theta < 170^\circ$, distance of closest Monte
 643 Carlo particle larger than 0.02 rad and production radius smaller than 50 mm. The low- p_T region is
 644 comparable with the one for Z-like bosons events. However, the efficiency for $b\bar{b}$ events reaches a
 645 maximum of 99% around 1 GeV and then decreases progressively at higher transverse momentum down
 646 to a minimum of 96%. Figure 45(b) shows that the fake rate is higher in the low- p_T region, due to the
 647 intrinsic difficulty to reconstruct low energetic particles, reaches a minimum at 1 GeV and increases
 648 again for higher momentum, as tracks are more straight and confusion in selecting hits from close-by
 649 particles arise. The maximum fake rate reached, however, is around 4%. Both efficiency and fake rates
 650 do not depend visibly on the background overlay.

651 Figure 46 shows the same efficiency (left) and fake rate (right) as a function of polar angle. The fol-
 652 lowing cuts are applied in Figure 46(a): $p_T > 1$ GeV, distance of closest Monte Carlo particle larger than
 653 0.02 rad and production radius smaller than 50 mm. The results show the correlation between efficiency

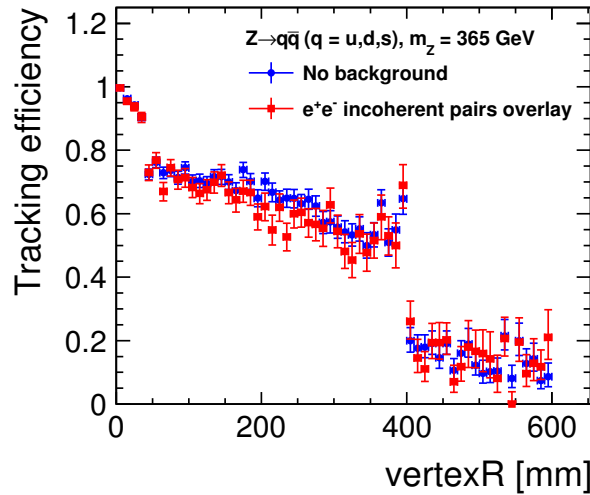


Figure 43: Tracking efficiency as a function of the production vertex radius for Z-like boson events decaying into light quarks, with $m_Z = 365$ GeV, with and without background overlay.

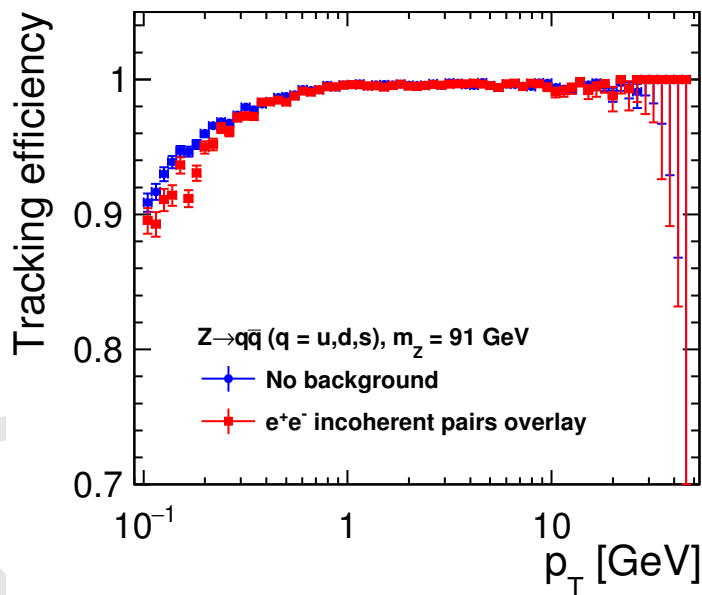


Figure 44: Tracking efficiency as a function of p_T for Z-like boson events decaying into light quarks, with $m_Z = 91.2$ GeV, with and without background overlay.

654 losses and fake rate increases.

655 Finally, in Figure 47 efficiency (left) and fake rate (right) are plotted as a function of production vertex
 656 radius. In Figure 47(a), the following cuts are applied: $p_T > 1$ GeV, $10^\circ < \theta < 170^\circ$ and distance of
 657 closest MC particle > 0.02 rad. The efficiency trend is comparable with the results previously discussed
 658 for low-momentum muons and Z-like boson events (Figure 34, Figure 43). The fake rate shows a peak
 659 in correspondance of the 20% efficiency drop after the first two vertex barrel layers, and then increases
 660 progressively as the production vertex radius is more displaced from the interaction point.

661 The effect of the background on the tracking performances also in these events is found to be negli-
 662 gible.

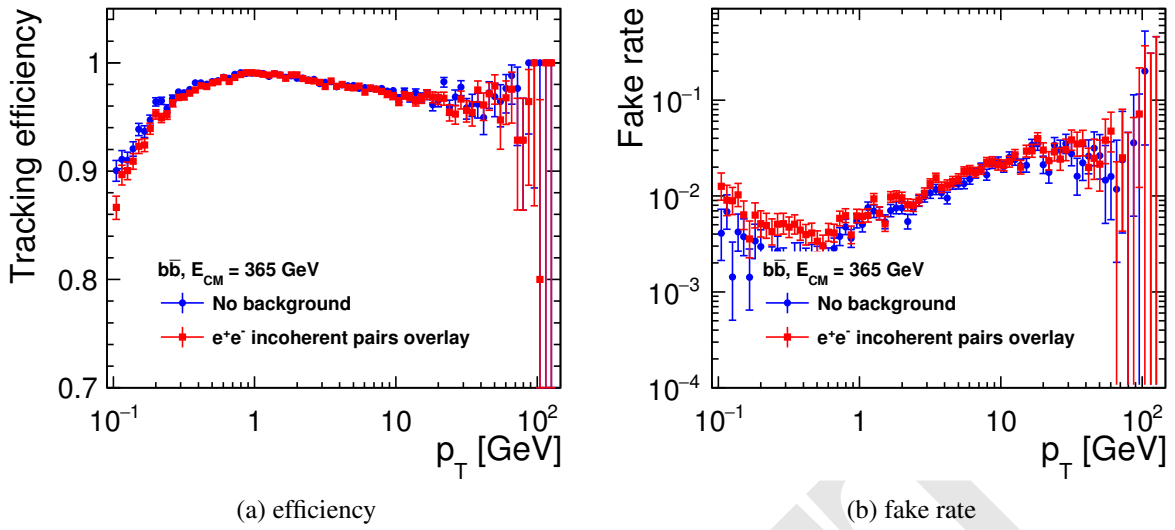


Figure 45: Tracking efficiency (a) and fake rate (b) as a function of transverse momentum for $b\bar{b}$ events at 365 GeV, with and without background overlay.

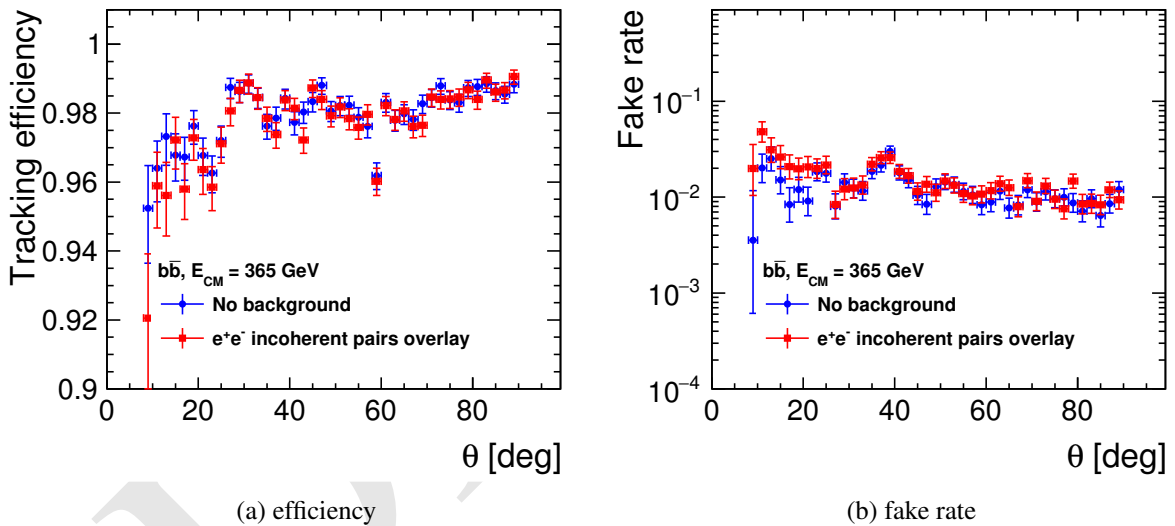


Figure 46: Tracking efficiency (a) and fake rate (b) as a function of θ for $b\bar{b}$ events at 365 GeV, with and without background overlay.

663 **Lepton Identification** Lepton identification efficiencies for muons and electrons have been studied for
 664 CLICdet in more complex $t\bar{t}$ samples at 3 TeV. In that study direct leptons from W decays were con-
 665 sidered. Muons were identified with more than 98% efficiency at all energies, and overlay of background
 666 had no impact on the result. The electron identification efficiency was found to be higher than 90% for
 667 electrons with more than 20 GeV energy.

668 The corresponding CLD studies on muon and electron identification in $t\bar{t}$ events at 365 GeV are in
 669 progress.

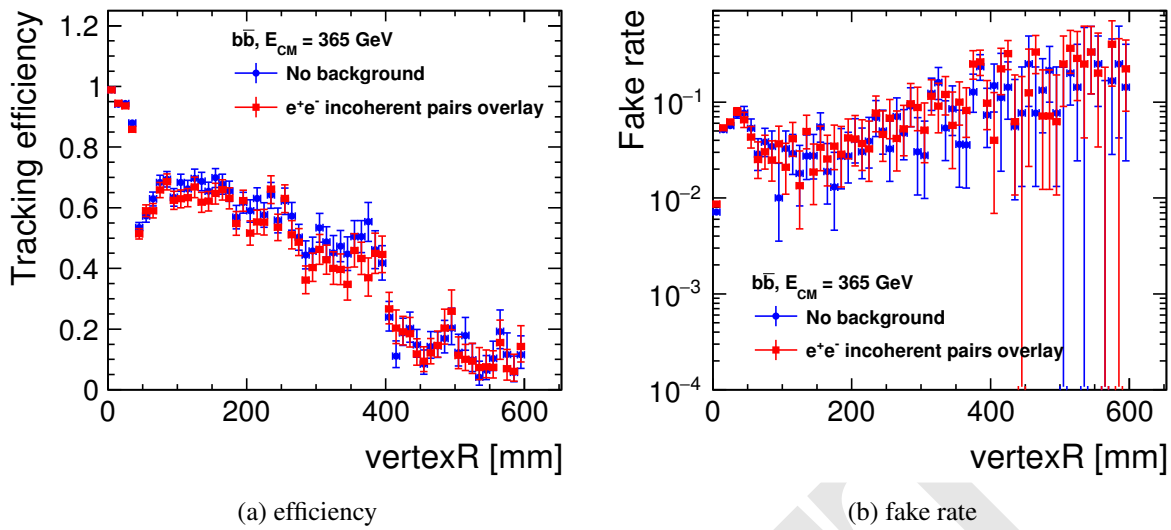


Figure 47: Tracking efficiency (a) and fake rate (b) as a function of production vertex radius for $b\bar{b}$ events at 365 GeV, with and without background overlay.

670 7.2.3 Jet Energy Resolution

671 The accurate jet energy resolution obtained using highly granular calorimeters and Particle Flow al-
 672 gorithms allow differentiating between different decays, e.g. between jets originating from W and Z
 673 boson decays. The jet performance in CLD is studied in dijet events using decays of a Z-like particle
 674 into light quarks (u, d, s) at two centre-of-mass energies. The Pandora particle flow algorithms [12, 37]
 675 are used to reconstruct each particle, combining information from tracks, calorimeter clusters and hits
 676 in the muon system. Software compensation is applied to clusters of reconstructed hadrons to improve
 677 their energy measurement, using local energy density information provided by the high granularity of
 678 the calorimeter system [39]. The jet energy resolution is determined using the energy sum of all recon-
 679 structed particles compared to the sum of all stable visible particles (excluding neutrinos) on MC truth
 680 level [40].

681 RMS_{90} is used as a measure for the jet energy resolution. RMS_{90} is defined as the RMS in the smallest
 682 range of the reconstructed energy containing 90% of the events [37]. This measure is a good repres-
 683 entation for the resolution of the bulk of events, while it is relatively insensitive to the presence of tails.
 684 Figure 48 shows that applying software compensation improves the energy resolution of jets significantly
 685 by 5-7%.

686 The jet energy resolution performance is studied as function of the $|\cos \theta|$ of the quark. As shown in
 687 Figure 49 for lower energies the jet energy resolution is within 4.5%–5%, while for the higher energy
 688 jets the resolution is better than 4%. The CLD performance studies for jets including overlay of beam-
 689 induced backgrounds are in preparation - given the very small number of $\gamma\gamma \rightarrow$ hadrons events at FCC-
 690 ee, and the low energies of incoherent pairs and hits from synchrotron radiation photons, no deterioration
 691 of the jet energy resolution is expected.

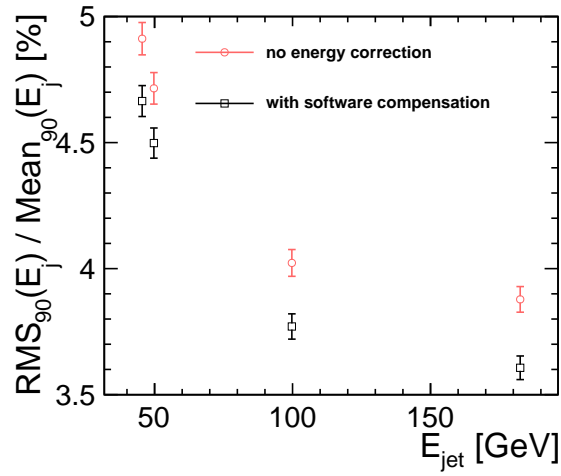


Figure 48: Jet energy resolution for central jets with $|\cos\theta| < 0.7$ as function of jet energy for events at different energies where a Z-like particle decays into two light (u, d, s) quarks. PFO reconstruction without energy correction (black) is compared to PFO reconstruction applying software compensation (red).

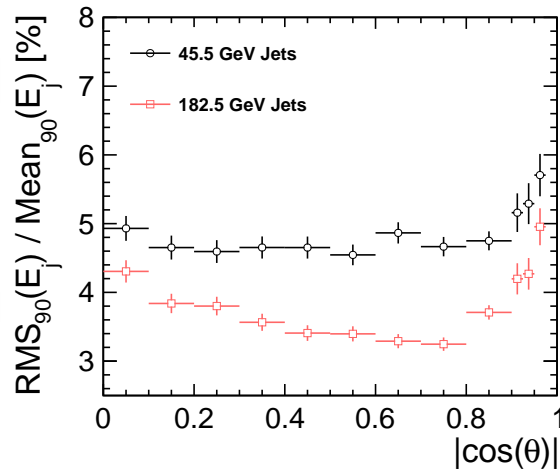


Figure 49: Jet energy resolution as a function of $|\cos\theta|$ for 45.5 and 182.5 GeV jets from a Z-like particle decaying into two light (u, d, s) quarks. PFO reconstruction with software compensation was used.

692 **7.2.4 Flavour Tagging**

693 Flavour tagging studies were initially performed for the CLIC_SiD detector model and described in
694 the CLIC CDR [3]. These studies were later extended to more realistic vertex detector geometries,
695 with particular emphasis on the material budget [41]. Recently, further studies were performed for the
696 CLICdet model, using the software chain described in 7.1 and the flavour tagging package LCFIPlus [42].

697 Work on flavour tagging in CLD, using the same tools and methodology, has started. It is expected
698 that the performance of CLD will be at least as good as the one of CLICdet - the smaller radius of the
699 innermost vertex barrel layer should lead to an improvement. On the other hand, the material added in
700 the vertex detector of CLD w.r.t. CLICdet might degrade the performance somewhat.

701 **8 Summary and Outlook**

702 A detector concept for FCC-ee, CLD, has been developed, based on the design of the CLIC detector
703 model (CLICdet). The detector features an all-silicon vertex and tracking system, followed by a silicon-
704 tungsten ECAL and a scintillator-steel HCAL. The detailed layout of the CLD concept, as implemented
705 in the simulation model, has been presented. First full simulation studies of CLD show promising per-
706 formance results.

707 One notable difference between CLICdet and CLD is the absence of power pulsing for the latter.
708 Future steps in the design of CLD will have to include detailed studies of the cooling, cabling and
709 supports of all subdetectors, not least the calorimeters. This implies detector optimisation by simulation
710 studies, but also a considerable engineering effort.

711 Additional engineering effort will have to be devoted to the integration of the detector parts, together
712 with the elements of the machine-detector interface (solenoids, quadrupoles, LumiCal, vacuum system,
713 etc.). Detector installation, opening and maintenance scenarios also need to be studied.

9 Appendix I: Overview of CLD sub-detector parameters and read-out channel numbers

In the following, sub-detector parameters for all CLD elements are given, together with the expected number of read-out channels. For the vertex and tracker discs, the numbers shown reflect the total (left plus right discs). Numbers for two scenarios are provided: In the first one, a tracker with strip geometry is assumed. The second scenario assumes (elongated) pixel geometry for the tracker, and is closer to the single point resolution assumed in the simulation model of CLD.

Table 16: Overview of CLD sub-detector parameters - a tracker with **strip geometry** is assumed.

Subdetector	Sensor area [m ²]	Cell size [mm ²]	Number of channels [10 ⁶]
VTX barrel	0.358	0.025×0.025	570
VTX petal discs	0.172	0.025×0.025	270
Inner Tracker Discs ITD1	1.27	0.025×0.025	2032
Inner Tracker Discs ITD2	2.66	0.05×1	54
Inner Tracker Discs ITD3	2.59	0.05×1	53
Inner Tracker Discs ITD4	2.47	0.05×1	50
Inner Tracker Discs ITD5	2.32	0.05×1	47
Inner Tracker Discs ITD6	2.03	0.05×1	41
Inner Tracker Discs ITD7	1.95	0.05×1	40
Outer Tracker Discs OTD1	23.94	0.05×10	49
Outer Tracker Discs OTD2	23.94	0.05×10	49
Outer Tracker Discs OTD3	23.94	0.05×10	49
Outer Tracker Discs OTD4	23.94	0.05×10	49
Inner Tracker Barrel ITB1	0.77	0.05×1	16
Inner Tracker Barrel ITB2	2.42	0.05×1	48
Inner Tracker Barrel ITB3	5.83	0.05×5	24
Outer Tracker Barrel OTB1	15.88	0.05×10	32
Outer Tracker Barrel OTB2	24.91	0.05×10	50
Outer Tracker Barrel OTB3	33.93	0.05×10	68
ECAL barrel	2498	5×5	99
ECAL endcaps (including ECAL plugs)	1486	5×5	59
HCAL barrel	3629	30×30	4.0
HCAL endcaps (including HCAL rings)	4750	30×30	5.2
MUON barrel	1916	30×30	2.1
MUON endcaps	1351	30×30	1.5

Table 17: Overview of CLD sub-detector parameters - a tracker with **pixel geometry** is assumed.

Subdetector	Sensor area [m ²]	Cell size [mm ²]	Number of channels [10 ⁶]
VTX barrel	0.358	0.025×0.025	570
VTX petal discs	0.172	0.025×0.025	270
Inner Tracker Discs ITD1	1.27	0.025×0.025	2032
Inner Tracker Discs ITD2	2.66	0.03×0.3	296
Inner Tracker Discs ITD3	2.59	0.03×0.3	294
Inner Tracker Discs ITD4	2.47	0.03×0.3	271
Inner Tracker Discs ITD5	2.32	0.03×0.3	256
Inner Tracker Discs ITD6	2.03	0.03×0.3	224
Inner Tracker Discs ITD7	1.95	0.03×0.3	219
Outer Tracker Discs OTD1	23.94	0.03×0.3	2725
Outer Tracker Discs OTD2	23.94	0.03×0.3	2725
Outer Tracker Discs OTD3	23.94	0.03×0.3	2725
Outer Tracker Discs OTD4	23.94	0.03×0.3	2725
Inner Tracker Barrel ITB1	0.77	0.03×0.3	88
Inner Tracker Barrel ITB2	2.42	0.03×0.3	266
Inner Tracker Barrel ITB3	5.83	0.03×0.3	663
Outer Tracker Barrel OTB1	15.88	0.03×0.3	1753
Outer Tracker Barrel OTB2	24.91	0.03×0.3	2754
Outer Tracker Barrel OTB3	33.93	0.03×0.3	3783
ECAL barrel	2498	5×5	99
ECAL endcaps (including ECAL plugs)	1486	5×5	59
HCAL barrel	3629	30×30	4.0
HCAL endcaps (including HCAL rings)	4750	30×30	5.2
MUON barrel	1916	30×30	2.1
MUON endcaps	1351	30×30	1.5

References

- [1] N. Alipour Tehrani et al., *CLICdet: The post-CDR CLIC detector model* (2017), CLICdp-Note-2017-001, URL: <https://cds.cern.ch/record/2254048>.
- [2] *FCC Conceptual Design Report* (2018).
- [3] L. Linssen et al., eds., *CLIC Conceptual Design Report: Physics and Detectors at CLIC*, CERN, 2012, arXiv: [1202.5940](https://arxiv.org/abs/1202.5940) [physics.ins-det].
- [4] *FCC-ee CDR Chapter describing the Machine Detector Interface and the Experimental Environment* (2018).
- [5] R. Erickson, *SLC Design Hand Book*, SLAC Document (1984).
- [6] A. Nurnberg, D. Dannheim, *Requirements for the CLIC tracker readout* (2017), CLICdp-Note-2017-002.
- [7] ALICE Collaboration, *Technical Design Report for the Upgrade of the ALICE Inner Tracking System*, J. Phys. G **41** (2014), ALICE-TDR-017 087002.
- [8] F. Duarte Ramos, *Conceptual Design and Prototyping of a Lightweight Support Structure Proposal for the Outer Barrel of the CLIC Detector Tracker*, EDMS document No. 1828030, 2016, URL: <https://edms.cern.ch/document/1828030/>.
- [9] S. Sroka et al., *New CLIC detector model - engineering input to the vertex and tracker layout*, EDMS document No. 1706383, 2016, URL: <https://edms.cern.ch/document/1706383/>.
- [10] M. A. Thomson, *Particle Flow Calorimetry and the PandoraPFA Algorithm*, Nucl. Instrum. Meth. **A611** (2009), arXiv:0907.3577 25, DOI: [10.1016/j.nima.2009.09.009](https://doi.org/10.1016/j.nima.2009.09.009), arXiv: [0907.3577](https://arxiv.org/abs/0907.3577) [physics.ins-det].
- [11] J. S. Marshall, M. Thomson, *The Pandora software development kit for particle flow calorimetry*, Journal of Physics: Conference Series **396** (2012) 022034.
- [12] J. Marshall, M. Thomson, *The Pandora Software Development Kit for Pattern Recognition*, Eur.Phys.J. **C75** (2015) 439, DOI: [10.1140/epjc/s10052-015-3659-3](https://doi.org/10.1140/epjc/s10052-015-3659-3), arXiv: [1506.05348](https://arxiv.org/abs/1506.05348) [physics.data-an].
- [13] F. Sefkow, et al., *Experimental tests of particle flow calorimetry*, Rev. Mod. Phys **88** (2016) 1.
- [14] K. Krueger, *Results from highly granular calorimeters developed by the CALICE collaboration*, CERN Detector Seminar, 2016, URL: <https://indico.cern.ch/event/563768/>.
- [15] N. Nikiforou, *Hadronic Calorimeter Optimization for a New Detector Model at CLIC, Draft Note, EDMS document No. 1756529*, 2016.
- [16] T. Behnke, et al., *The International Linear Collider Technical Design Report - Volume 4: Detectors*, CERN-ATS-2013-037, 2013.
- [17] K. Krueger, *Cooling of ECAL and HCAL*, Presented at the CLICdp workshop, 2017, URL: https://indico.cern.ch/event/633975/contributions/2686140/attachments/1514660/2363321/Cooling_CLICdp_20170829.pdf.
- [18] D. Grondin, J. Giraud, J.-Y. Hostchy, *CALICE Si/W ECAL: Endcap structures and cooling system* (2016), Talk presented at LCWS2016, URL: [arXiv:1702.03770v1](https://arxiv.org/abs/1702.03770v1).

- 762 [19] D. Grondin, K. Krueger, J. Giraud,
763 *Design of cooling systems for tungsten / carbon fibre and for hadron calorimeter structures*
764 (2016), AIDA-2020 Milestone Report,
765 URL: <http://cds.cern.ch/search?p=AIDA-2020-MS31>.
- 766 [20] D Grondin, K Krueger, J Giraud, *Large leak-less system, thermal model*
767 (2018), AIDA-2020 Deliverable Report D14.8.
- 768 [21] *The Phase-2 Upgrade of the CMS Endcap Calorimeter (Technical Design Report)*
769 (2017), CERN-LHCC-2017-023.
- 770 [22] *FCC-ee CDR Chapter describing the Superconducting Solenoid of the FCC-ee Detector*
771 *Concepts* (2018).
- 772 [23] M. Frank et al., *DD4hep: A Detector Description Toolkit for High Energy Physics Experiments*,
773 J. Phys. Conf. Ser. **513** (2013) 022010.
- 774 [24] *AIDA Common Software Tools*, URL: <http://aidasoft.web.cern.ch/>.
- 775 [25] A Tsaregorodtsev et al., *DIRAC: a community grid solution*,
776 J. Phys.: Conf. Ser. **119** (2008) 062048, URL: <https://cds.cern.ch/record/1176117>.
- 777 [26] C. Grefe et al., *ILCDIRAC, a DIRAC extension for the Linear Collider community*,
778 J. Phys. Conf. Ser. **513** (2013), CLICdp-Conf-2013-003 032077,
779 DOI: [10.1088/1742-6596/513/3/032077](https://doi.org/10.1088/1742-6596/513/3/032077).
- 780 [27] W. Kilian, T. Ohl, J. Reuter, *WHIZARD: Simulating Multi-Particle Processes at LHC and ILC*,
781 Eur.Phys.J. C **71** (2011) 1741, arXiv: [0708.4233 \[hep-ph\]](https://arxiv.org/abs/0708.4233).
- 782 [28] M. Moretti, T. Ohl, J. Reuter, *O'Mega: An optimizing matrix element generator*, 2001,
783 arXiv: [0102195 \[hep-ph\]](https://arxiv.org/abs/0102195).
- 784 [29] S. Agostinelli et al., *Geant4 – A Simulation Toolkit*, Nucl. Instrum. Methods A **506** (2003) 250,
785 DOI: [10.1016/S0168-9002\(03\)01368-8](https://doi.org/10.1016/S0168-9002(03)01368-8).
- 786 [30] J. Allison et al., *Geant4 developments and applications*, IEEE T. Nucl. Sci. **53** (2006) 270,
787 DOI: [10.1109/TNS.2006.869826](https://doi.org/10.1109/TNS.2006.869826).
- 788 [31] J. Allison et al., *Recent developments in Geant4*, Nucl. Instrum. Methods A **835** (2016) 186,
789 DOI: [10.1016/j.nima.2016.06.125](https://doi.org/10.1016/j.nima.2016.06.125).
- 790 [32] M. Frank et al.,
791 *DDG4: A Simulation Framework using the DD4hep Detector Description Toolkit*,
792 J. Phys. Conf. Ser. **664** (2015) 072017.
- 793 [33] F. Gaede, *Marlin and LCCD: Software tools for the ILC*, Nucl. Instrum. Meth. **A559** (2006) 177.
- 794 [34] A. Sailer et al., *DD4Hep Based Event Reconstruction*, J. Phys. Conf. Ser. **898** (2017) 042017.
- 795 [35] P. Schade, A. Lucaci-Timoce, *Description of the signal and background event mixing as*
796 *implemented in the Marlin processor OverlayTiming*, CERN LCD-Note-2011-006, 2011.
- 797 [36] E. Leogrande, *Conformal tracking for the CLIC detector*,
798 EPJWeb (2018), CLICdp-Note-2018-XYZ, in preparation.
- 799 [37] J. S. Marshall, A. Münnich, M. Thomson, *Performance of Particle Flow Calorimetry at CLIC*,
800 Nucl. Instrum. Meth. **A700** (2013) 153, DOI: [10.1016/j.nima.2012.10.038](https://doi.org/10.1016/j.nima.2012.10.038),
801 arXiv: [1209.4039 \[physics.ins-det\]](https://arxiv.org/abs/1209.4039).
- 802 [38] C. Adloff, et al, *Hadronic energy resolution of a highly granular scintillator-steel hadron*
803 *calorimeter using software compensation techniques*, JINST **7** (2012) P09017.

- 804 [39] H. Tran et al., *Software compensation in Particle Flow reconstruction*,
805 Eur. Phys. J. **C77** (2017) 698, DOI: [10.1140/epjc/s10052-017-5298-3](https://doi.org/10.1140/epjc/s10052-017-5298-3),
806 arXiv: [1705.10363](https://arxiv.org/abs/1705.10363) [physics.ins-det].
- 807 [40] C. Buttar et al.,
808 *Standard Model Handles and Candles Working Group: Tools and Jets Summary Report*, Physics
809 at TeV colliders, La physique du TeV aux collisionneurs, Les Houches 2007 : 11-29 June 2007,
810 2008, p. 121, arXiv: [0803.0678](https://arxiv.org/abs/0803.0678) [hep-ph],
811 URL: <https://inspirehep.net/record/780755/files/arXiv:0803.0678.pdf>.
- 812 [41] N. Alipour Tehrani, *Optimisation studies for the CLIC vertex-detector geometry*
813 (2015), CLICdp-Conf-2015-002.
- 814 [42] T. Suehara, T. Tanabe, *LCFIPlus: A Framework for Jet Analysis in Linear Collider Studies*,
815 Nucl. Instrum. Meth. **A808** (2016) 109, DOI: [10.1016/j.nima.2015.11.054](https://doi.org/10.1016/j.nima.2015.11.054),
816 arXiv: [1506.08371](https://arxiv.org/abs/1506.08371) [physics.ins-det].